SEPTEMBER 2019 M.Sc. in Electrical and Electronics Engineering Hüseyin KORKMAZ

REPUBLIC OF TURKEY

GAZİANTEP UNIVERSITY

GRADUATE SCHOOL OF NATURAL & APPLIED SCIENCES

THE USE AND INVESTIGATION OF TWO-DIMENSIONAL MATERIALS IN SOLAR CELLS

M.Sc. THESIS

IN

ELECTRICAL AND ELECTRONICS ENGINEERING

BY

HÜSEYİN KORKMAZ

SEPTEMBER 2019

THE USE AND INVESTIGATION OF TWO-DIMENSIONAL MATERIALS IN SOLAR CELLS

M.Sc. Thesis

in

Electrical and Electronics Engineering

Gaziantep University

Supervisor

Prof. Dr. Uğur Cem HASAR

by

Hüseyin KORKMAZ

September 2019

REPUBLIC OF TURKEY
GAZİANTEP UNIVERSITY
GRADUATE SCHOOL OF NATURAL & APPLIED SCIENCES
DEPARTMENT'S NAME

Name of the Thesis : The Use and Investigation of Two-dimensional Materials in Solar cells

Name of the Student : Hüseyin KORKMAZ

Exam Date : 04.09.2019

Approval of the Graduate School of Natural and Applied Sciences

Prof. Dr. A. Necmeddin YAZICI
Director

I certify that this thesis satisfies all the requirements as a thesis for the degree of Master of Science.

Prof. Dr. Ergun ERÇELEBİ
Head of Department

This is to certify that we have read this thesis and that in our consensus opinion it is fully adequate, in scope and quality, as a thesis for the degree of Master of Science.

Prof. Dr. Uğur Cem HASAR
Supervisor

Examining Committee Members:	Signature
Prof. Dr. Uğur Cem HASAR	…………………..
Prof. Dr. Kemal DELİHACIOĞLU	…………………..
Dr. Musa BUTE	…………………..

I hereby declare that all information in this document has been obtained and presented in accordance with academic rules and ethical conduct. I also declare that, as required by these rules and conduct, I have fully cited and referenced all material and results that are not original to this work.

Hüseyin KORKMAZ

ABSTRACT

THE USE AND INVESTIGATION OF TWO-DIMENSIONAL MATERIALS IN SOLAR CELLS

KORKMAZ, Hüseyin
M.Sc. in Electrical and Electronics Engineering
Supervisor: Prof. Dr. Uğur Cem HASAR
September 2019
78 pages

Solar cells do not have ability to absorb the majority of the electromagnetic waves that are coming towards them. Our aim is using MXene which is a new member of two-dimensional (2D) materials family to increase the solar cells efficiency by increase the absorption coefficient. We designed, simulated and analyzed MXene metamaterial absorber in the visible frequency region for solar cell applications. Titanium carbide ($Ti_3C_2T_x$) was used as a dielectric layer of proposed solar cell absorber. Electromagnetic response of the proposed design is computationally analyzed using a full-wave electromagnetic solver simulation program. Geometric parameters of design were carefully analyzed to show absorption behavior of proposed design. The proposed design provide maximum of 96.8 % absorption and it is independent from normal incidence (transverse electromagnetic mode), so proposed design can be good candidate for the solar cell applications.

Key Words: Mxene, Solar Cell, Efficiency, Wide Band Absorber, Visible Frequency

ÖZET

GÜNEŞ HÜCRELERİNDE İKİ BOYUTLU MALZEMELERİN KULLANILMASI VE İNCELENMESİ

KORKMAZ, Hüseyin
Yüksek Lisans Tezi, Elektrik Elektronik Mühendisliği
Danışman: Prof. Dr. Uğur Cem HASAR

Eylül 2019
78 sayfa

Güneş pilleri, kendilerine gelen elektromanyetik dalgaların çoğunu emme yeteneğine sahip değildir. Amacımız iki boyutlu malzeme ailesinin yeni üyesi olan MXene malzemesini kullanıp soğurma katsayısını artırarak güneş hücrelerinin verimliliğini arttırmaktır. Solar hücre uygulamaları için görülür frekans bölgesinde MXene metamalzeme emicisini tasarlayarak simulasyon ve analizini yaptık. Titanyum karbür ($Ti_3C_2T_x$) önerilen güneş pili emicisinin dielektrik tabakası olarak kullanılmıştır. Önerilen tasarımın elektromanyetik tepkisi, bir tam dalga elektromanyetik çözücü simülasyon programı kullanılarak hesaplamalı olarak analiz edilmiştir. Tasarımın geometrik parametreleri, önerilen tasarımın soğurma davranışını göstermek için dikkatlice analiz edildi. Önerilen tasarım geniş bantta maksimum 96.8 % soğurma ve enine elektromanyetik mod etkisinde bağımsız geniş bant saglamaktadır. Önerilen tasarım güneş pili uygulamalar için iyi bir adaydır.

Anahtar Kelimeler: Mxene, Güneş Pili, Verimlilik, Geniş Bant Sogurucusu, Görülür Frekans

''Dedicated to my family''

ACKNOWLEDGMENTS

During this study, I would like to express my best wishes to my supervisor Prof. Dr. Uğur Cem HASAR who supported me with his academic knowledge, recommendations, and encouragements.

In addition, I would like to thank my colleague Hamdullah ÖZTÜRK and Emine KILINÇ who supported me in the study process, and my dear friends who helped me in my study.

I would like to thank my dear friends Furkan Cemal SAVAŞ, Selman YAVUZ and Ali Alper DEGER for their supports.

I would like to thank my dear uncle Mehmet KORKMAZ, who has always motivated and supported me.

Finally, I am thankful to my dear mother Nahide KORKMAZ and my father pharmacist Salih KORKMAZ who educate me, for their all kinds of moral and material supports.

TABLE OF CONTENTS

Pages

LIST OF TABLES

Pages

LIST OF FIGURES

Pages

LIST OF SYMBOLS

μ	Mu
λ	Lamda
Ω	Ohm
Ɛ	Epsilon
Ɵ	Theta
Φ	Phi

LIST OF ABBREVIATIONS

f	Frequency
nm	Nanometre
c	Speed of light
THz	Terahertz
TMD	Transition Metal Dichalcogenide
2D	Two-Dimensional
TE	Transverse Electric
TM	Transverse Magnetic
TEM	Transverse Electromagnetic
PV	Photovoltaic
MMs	Metamaterials
CNT	Carbon nanotube
CST	Computer Simulation Technology
SWNT	Single Walled Carbon Nanotube
MWNT	Multi walled Carbon Nanotube

CHAPTER 1
1.INTRODUCTION

1.1.Background and Motivation of Thesis

The technological developments that we have in the 21.century offer us a more comfortable life with increased energy demand day by day. This situation is expressed by many countries, institutions, and researchers in every platform. Energy plays an important role in the industrial and financial development of each country. Researchers take attention to the production and usage of sustainable and renewable energy and protection of the environment and natural resource [1].

Energy source is a lead of source that can be obtained with economic purposes by using various methods and techniques. Renewable (alternative) energy sources are defined by the ability to renew itself at the same rate as the energy from the source, or faster than the rate of depletion of the source. Hydroelectric energy, wind energy, solar energy, biomass energy, geothermal energy, wave energy and tidal energy can be listed as renewable energy sources. Although the techniques of use of nature as fuel can change, basically all sources of energies are the sun. The most striking feature of non-renewable (fossil, conventional, traditional) energy source is that they cannot be renewable, that is, they can be used once and they are depleted [2].

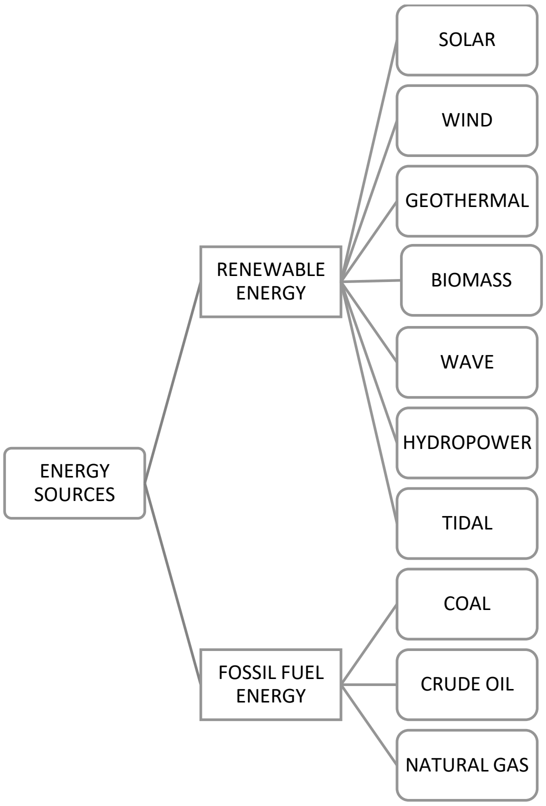

Figure 1. 1 Types of Energy Sources [2].

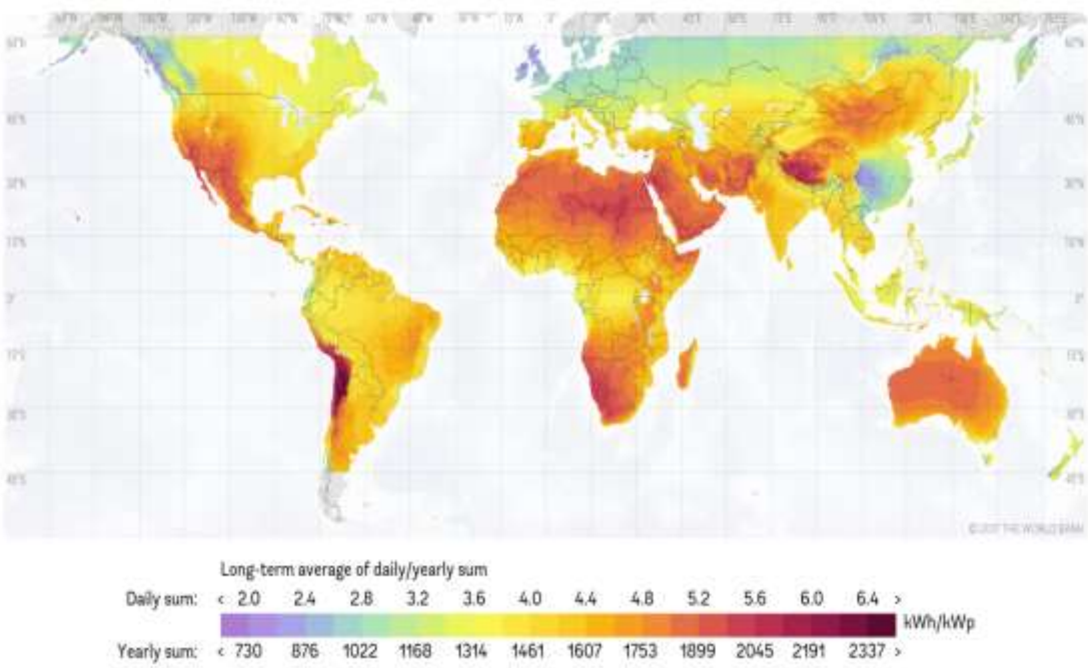

Figure 1.2 The photovoltaic power potential of the world.

Turkey is located between 36° - 42° north parallels and 26° - 45° east meridians [54]. Due to the geographical location of Turkey, the potential to benefit from solar energy is quite high. According to data that taken from T.C Ministry of Energy and Natural Resources, Turkey has 7.5 hours sunshine duration per day, and 1.527 kWh/m2 total annual incoming solar energy in a year. It was determined according to 4,2 kWh/m2 (daily total) per year. Turkey has solar energy potential for approximately 114 days [55]. These values show that Turkey has a high potential among Europe and other countries.

People have needed energy since the world existed. However, people are not content with what they have and always be in search of a new energy source. Although fossil fuels are limited and environmentally harmful, fossil fuels have an important rate among consumed energy sources. Despite, many countries are focusing on renewable energy, trying to reduce environmental pollution and research on alternative energy sources are promising for the future of energy [4].

In this section, you will find information about the different energy sources and quantities consumed in some years. The following figures in Figure 1.3 show that the amount of energy consumed in the world is increasing by years. There is also a noticeable increase in renewable energy consumption.

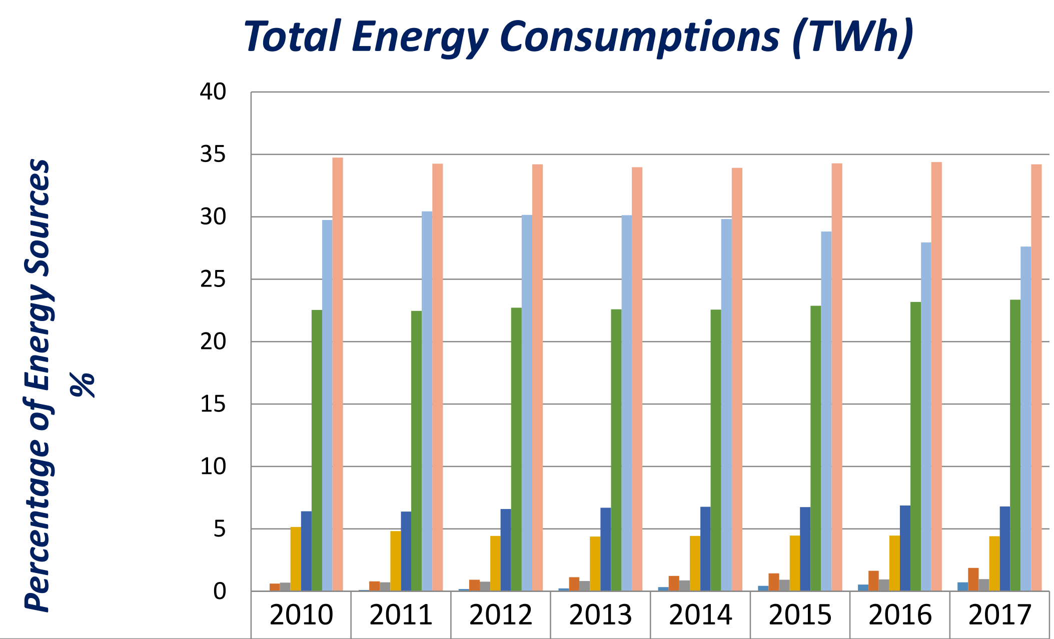

	2010	2011	2012	2013	2014	2015	2016	2017
solar	0,06	0,12	0,18	0,25	0,35	0,45	0,56	0,74
wind	0,64	0,8	0,94	1,14	1,24	1,44	1,64	1,88
other renewable	0,71	0,72	0,77	0,82	0,88	0,93	0,95	0,98
nuclear	5,17	4,83	4,44	4,39	4,44	4,46	4,46	4,41
hydropower	6,41	6,39	6,6	6,7	6,79	6,74	6,89	6,8
natural gas	22,53	22,45	22,72	22,6	22,56	22,87	23,18	23,36
coal	29,75	30,44	30,14	30,13	29,81	28,83	27,95	27,62
crude oil	34,73	34,25	34,2	33,98	33,93	34,27	34,37	34,21

Figure 1.3 Percentage Share of Each Resource in Total Energy Consumed [3].

The percentage of total energy consumed in the world is compared with the years. According to this graph, the percentage share of renewable energy (solar, wind, other renewable and hydropower) in total energy consumption has increased compared to 2010 and 2017. In addition, if we compare the values between 2010 and 2017, the share of non-renewable energy (nuclear, natural gas, coal, and crude oil) in total energy consumption has decreased. The result is that the world's interest in renewable energy has increased over the years.

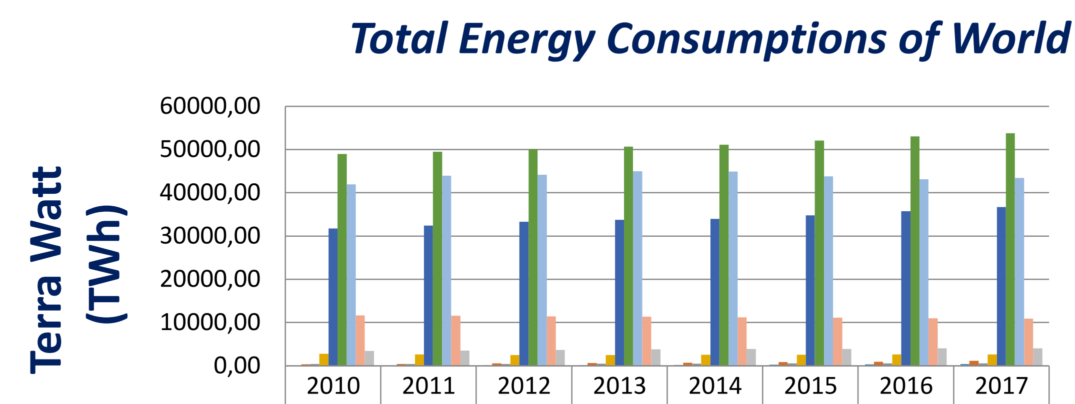

	2010	2011	2012	2013	2014	2015	2016	2017
solar	33,83	65,21	100,93	139,04	197,67	260,01	328,18	442,62
wind	341,57	436,80	523,81	645,72	712,41	831,83	959,47	1122,75
other renewables	378,04	397,45	430,36	463,98	504,39	538,21	556,99	586,17
nuclear	2767,51	2651,77	2472,45	2491,71	2541,03	2575,66	2612,83	2635,56
natural gas	31759,1	32410,4	33270,5	33714,9	33986,8	34741,8	35741,8	36703,9
crude oil	48949,7	49455,2	50065,8	50698,3	51109,9	52053,2	53001,8	53752,2
coal	41932,7	43948,9	44129,6	44953,0	44916,8	43786,8	43101,2	43397,1
traditional biofuels	11666,6	11553,3	11441,1	11330,0	11220,0	11111,1	11003,2	10895,3
Hydropower	3435,91	3503,23	3671,30	3797,95	3887,93	3891,41	4036,07	4059,87

Figure 1.4 Total energy consumption of the world with different energy sources distribution [3].

The share of the total energy consumed in the world compared to the years in Terra Watt (TWh) is indicated in Figure 1.4. We can do analysis by taking the values between 2010 and 2017 as a reference. Firstly, while solar energy consumed 33.83 terawatt-hours in 2010, in 2017 it consumed 442.62 terawatt hours. From this point of view, solar energy consumption in the world increased nearly 13 times within seven years. While wind energy was consumed in 2010 at 341,57 terra watt hours, in 2017 this amount increased to 1122,75 terra watt hours. (approximately 3,3 times). Other renewables (biofuels, geothermal, wave and tidal energy) were consumed 378,04 terra watt hours in 2010, it has increased at 586,17 terra watt hours (approximately 1,6 times) were consumed in 2017. While hydropower energy consumed 3435.991 Terra Watts in 2010, it reaches 4059.87 terra watt hour energy consumed in 2017 (increased approximately % 18).

In addition, nuclear energy consumed 2767,51 Terra Watts hours in 2010, while 265,56 terra watts were consumed in 2017 (decreased approximately %4,8). Traditional biofuels (fuelwood, forestry products, animal and agricultural wastes) consumptions are decreased by approximately % 6,6 in case of taking reference 2010 and 2017 years.

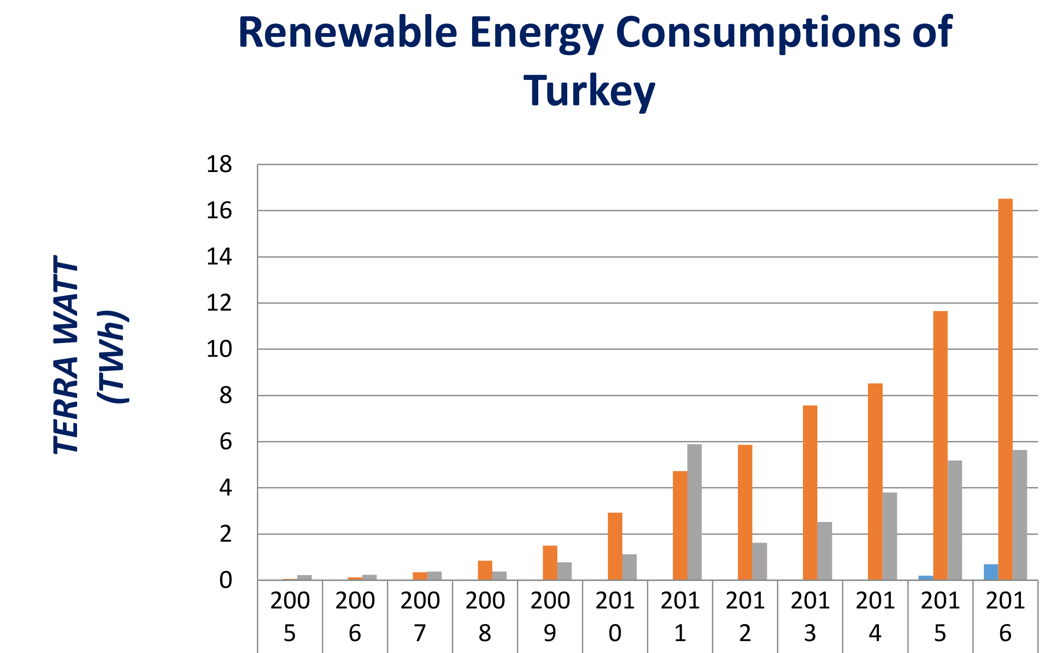

	2005	2006	2007	2008	2009	2010	2011	2012	2013	2014	2015	2016
solar	0	0	0	0	0	0,01	0,01	0,01	0,01	0,02	0,19	0,69
wind	0,06	0,13	0,35	0,85	1,5	2,92	4,72	5,86	7,56	8,52	11,65	16,52
other renewable	0,22	0,24	0,37	0,38	0,78	1,13	5,89	1,62	2,53	3,8	5,18	5,64

Figure 1.5 Total renewable energy consumption of Turkey with different renewable energy sources distribution per years [3].

Information about the consuming of renewable energy in Turkey between 2005 and 2016 is indicated in Figure 1.5. Until 2010 we can say that the production and consumption of solar energy were inactive. Solar energy rapidly becomes widespread since 2015 and consuming of wind energy has the largest share among renewable energy in Turkey

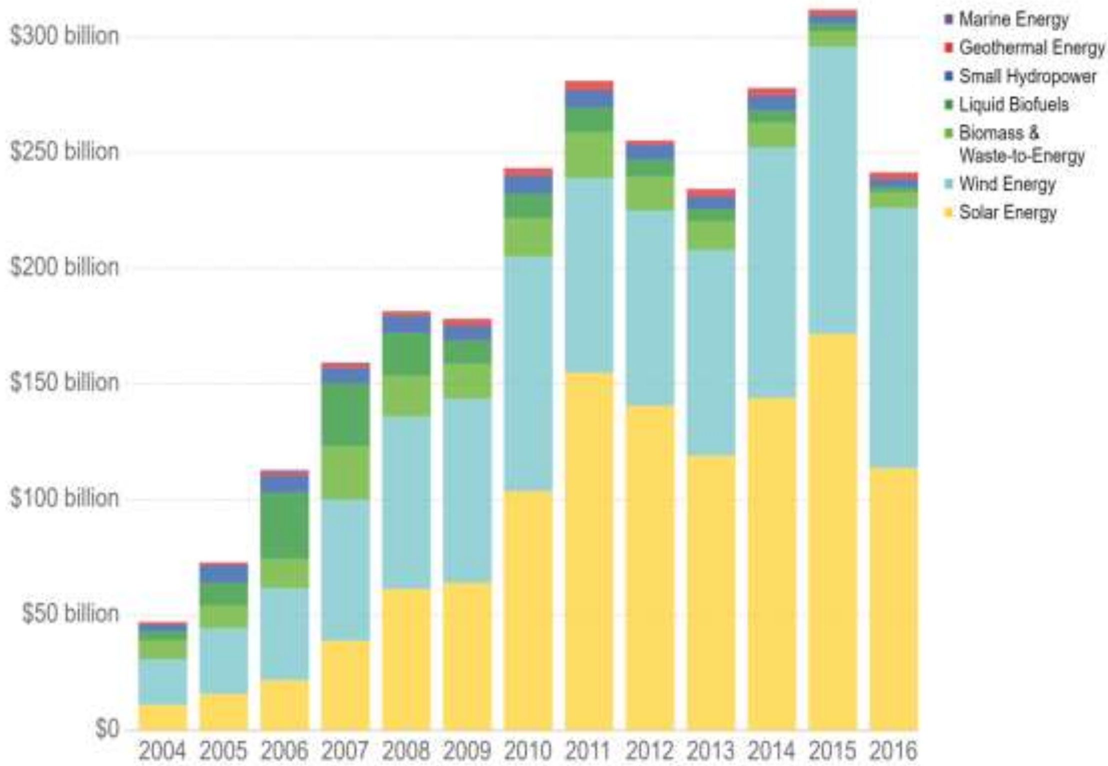

Figure 1. 6 Global investment in renewables technology by years [3].

In 2016, 47 % of investments were invested in solar and wind energy. This rate is equal to % 94 of global finance. The share of these two technologies especially in the last five years has increased. In 2006, bioenergy (biomass and liquid biofuels) rose to 36 percent by taking a large share of global investment. However, in 2016, it decreased by less than 4% of the investments. These data and analyses show that investors have idea about solar and wind energy is the dominant renewable technologies of the future.

The data obtained from various sources and the analysis in the light of the data above, it is understood that the tendency towards worldwide about solar energy consumption is increasing day by day. However, the use of photovoltaic panels is limited due to the fact that the solar cell, which is one of the main components of photovoltaic energy, has not yet reached a sufficient level of efficiency [5]. There are several reasons why the solar cells and solar panels have not yet reached a sufficient level of efficiency. These can be listed as reflection and shadow effect losses, long electromagnetic wave radiation with low energy losses, short electromagnetic wave radiation with high energy losses, recombination losses and ohmic losses in transition region. Long electromagnetic wave radiation with low energy losses, short electromagnetic wave radiation with high energy losses are important in the overall losses that reduce solar cell efficiency. From this point of view due to solar cells do not have the ability to absorb great majority of solar radiation coming towards them, the efficiency of solar cells remains low [6]. So what can we offer as a solution?

Solar cell absorber absorbs the sun's rays and produces more energy to increase efficiency of solar cells. Solar cell absorber is as important to the solar cell as it is to which material it is made. Recently emphasized that two-dimensional (2D) materials have the potential can solve this problem. Since the exploration of graphene a decade ago, 2D materials have been an important materials in research and engineering because of their properties such as outstanding electrical properties with a high carrier-mobility, high durability and high electrical conductivity [7]. Graphene, Carbon nanotube, TMDs, and MXene are member of two-dimensional materials. Graphene and carbon nanotube were used as active materials in solar cell absorber. Rufangura et al. designed metamaterial absorber with a graphene monolayer sheet located top of GaAs dielectric layer under circular concentric ring resonators and analyzed in 500-700 THz frequency region [8]. Obaidullah et al. designed a single-walled carbon nanotube metamaterial absorber consisting of a ground plate with metallic aluminum, carbon nanotube used as dielectric layer and aluminum resonator at the top of the dielectric and working in visible and ultraviolet frequency regions [9]. Since MXene has just been discovered, there are not so many scientific publications on MXene [10]. Therefore, it is a material open to scientific researches and investigations. MXene as the last member of two-dimensional materials has previously been applied to different types of solar cells as high electrical conductor in perovskite solar cells and used as electrodes for dye-sensitized solar cells [11][12]. However MXenes have not been studied in visible frequency for solar cell absorbers. Although solar radiation range between 100 and 1000 THz, much of energy being localized between 400 and 750 THz [13]. It shows that visible frequency region is important for solar cell applications.

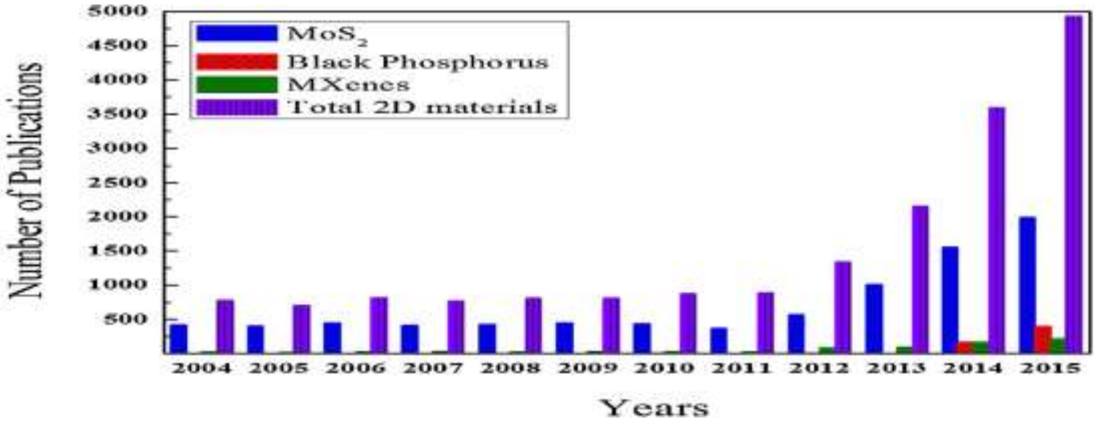

Figure 1.7 Publication plots for 2D TMDs including MoS2, MoSe2, black phosphorus, MXenes and total 2D TMDs in the period of 2004–2015 [10].

To our best knowledge, Titanium Carbide ($Ti_3C_2T_x$) MXene absorbers have been applied to optimize maximum absorption capacity of solar cells. In this study, we design a new solar cell absorber with $Ti_3C_2T_x$ MXene sandwiched between an aluminum resonator and an aluminum ground plate. The optical properties of the proposed design has been simulated in visible frequency region for incident wave with TE, TM, and TEM modes with different polarization angles. It has been demonstrated that the proposed design has high absorption capacity and thus can be considered as a good candidate for solar cell applications.

The remaining part of this thesis is as follows:

The aim of Chapter 2 is to explain the fundamentals of solar cells and 2D materials. In addition classification and application of an engineered material are described. Physics behind absorption, TE, TM and TEM mode are explained.

Chapter 3 presents how we obtain dielectric constants of Titanium Carbide($\mathrm{Ti_3C_2T_x}$) MXene, the details of the proposed design and its implementaition steps, simulation results of proposed absorber such as absorption-reflection curves, plots of TE, TM and TEM modes with different polarization angles and fields distribution of proposed design. Main goal of this chapter is to understand design steps of the new proposed absorber from implemented in simulation to discuss results of simulation.

In the Chapter 4, we briefly summarized the studies done during this thesis and mentioned about the some contributions to the scientific literature. Also we give information about the further studies that could be conducted the future.

CHAPTER 2
MATERIALS AND METHOD

2.1 Solar Cells

A solar cell is an electronic device working as a semiconductor diode which transform the energy of sunlight directly into electrical energy by utilizing the internal photoelectric reaction. The other name of the solar cell is photovoltaic (PV) cells. Photo process is related to light and voltaic action is related to electricity [46].

2.1.1 History of Solar Cells

Edmund Becquerel was a French physicist who first mentioned about the physical phenomenon of converting light to electricity. He claimed that voltage will be produce when two identical electrodes are immersed into a weak conducting solution and one electrode is illuminated. In the 1870s, the topic of photovoltaic effect was first studied in selenium. 1%-2% efficiency selenium photovoltaic cells were built to converting light to electricity. Thanks to selenium which converts visible light of solar spectrum, it was applied in the field of photography for light measuring devices. Using the method of Czochralski, highly pure crystalline silicon was produced in the 1940s and early 1950s. In 1954, researchers at Bell laboratories product silicon photovoltaic cells with an efficiency of 4 %. Silicon photovoltaics solar cells are later applied for the industrial field in the 1950s. In 1958, Vanguard space satellite used an array of cells which is less than one watt to power its radio [14].

2.1.2 Operation and PN Junction of Solar Cells

PN junction is a composition of n-type semiconductor and p-type semiconductor to reach the practical utility of both of them. P-type semiconductor has holes which are positively charged and n-type semiconductor has electrons which are negatively charged. The medium region as indicated in the Figure 2.1 is pn junction where the p-type and n-type are joined, R(0) represent resistive load and sun rays are the source of system.

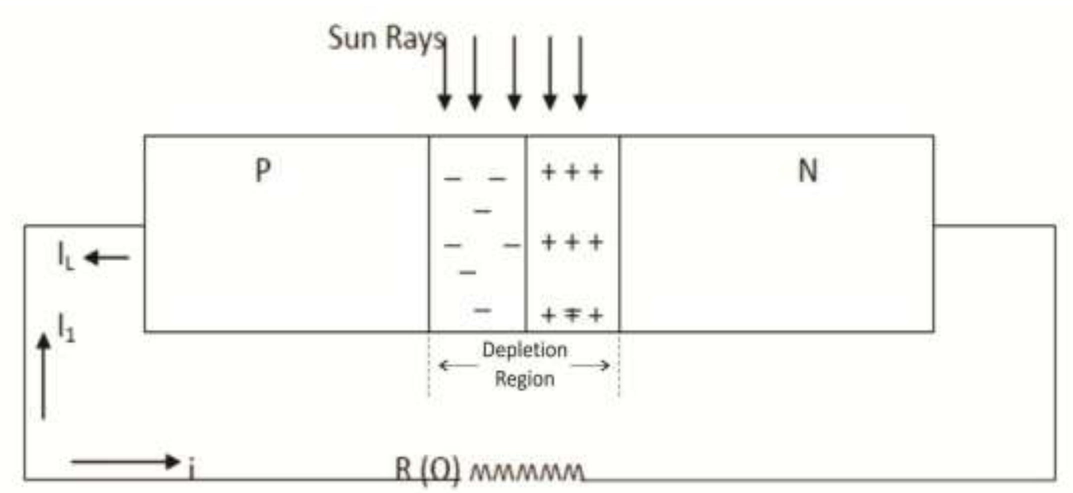

Figure 2. 1 Representation of pn junction of solar cells [15].

Electrons near the junctions jumped from n-type semiconductor towards p-type semiconductor and holes near the junctions jumped from p-type semiconductor towards n-type semiconductor. This phenomenon creates a depletion region at the junction. Electrons are available in p region at depletion region and holes are available in the n region at depletion region. The electric field is created in the depletion region because of the movement of the holes and electrons. The direction of the electric field is from the n-type region towards the p-type region. Some electrons move back from p region to n region in the depletion region, some holes move back from n region towards p region in the depletion region. This will continue until reaching the equilibrium at the depletion region. These movements of electrons and holes in the depletion region give rise to diffusion current.

In forward biasing positive terminal of battery connected to p region of the pn junction and the negative terminal of battery connected to n region of the pn junction.

Positive terminals repels the holes in the p region and the negative terminal repels electrons toward the junction in the n region. Due to this repulsion, the depletion region narrows down. When the voltage in the forward bias, the electrons in the n region flows through the junction and pass to the p region and the holes in the p region flows through the junction and pass to the n region. On the other hand, in reverse biasing, the battery is connected with the negative terminal to n region and a positive terminal connected to p region. Holes get away to the negative side of the battery and electrons get away to the positive side of the battery. This situation resulted in an increase of the depletion layer and pn junction act as an insulator which does not allow any current to flow in the circuit. If the battery voltage above the particular limit, electrons and holes breakdown through the pn junction and resulted with current flowing through the circuit. During this process, the current through the pn junction is very high and due to overheating caused by the excess flow of current the pn junction gets damaged [16].

When a solar cell is illuminated, electron hole pair is generated in the depletion region. This electron hole pair when separated from each other across junction produces a current I_L flowing in external circuit by photovoltaic effect. This photo current I_L creates a voltage drop across resistive load and this voltage will forward bias the pn junction. Forward bias voltage produces forward current I_1, so the net current shown in equation (2.1) and kT is product of Boltzmann constant k and temprature T, eV is short term of electron volt that is approximately equal to 1,6x10^{-19} joule [2].

$$i = I_L - I_1 \quad (2.1)$$

$$I_1 = I(0)[\exp(\frac{eV}{kT}) - 1] \quad (2.2)$$

$$i = I_L - I(0)[\exp(\frac{eV}{kT}) - 1] \quad (2.3)$$

2.1.3 Parameters of Solar Cells

When R=0 and V = 0 then I_1 =0, so

$$i = I_L = I_{sc} \qquad (2.4)$$

Open circuit voltage (V_{oc}) of solar cell can be found as following

When R=∞ , then i = 0 so,

$$0= i=I_L-I(0)[\exp(\frac{eV}{kT})-1] \qquad (2.5)$$

$$I_L= I(0)[\exp(\frac{eV}{kT})-1] \qquad (2.6)$$

$$V_{oc} = \frac{kT}{e}[\ln(1+\frac{I_L}{I(0)})] \qquad (2.7)$$

Since power delivered to load is the multiplication of V and i, we obtain i from equation (2.5) and substitute in equation (2.8)

$$P=V.[I_L-I(0)[\exp(\frac{eV}{kT})-1]] \qquad (2.8)$$

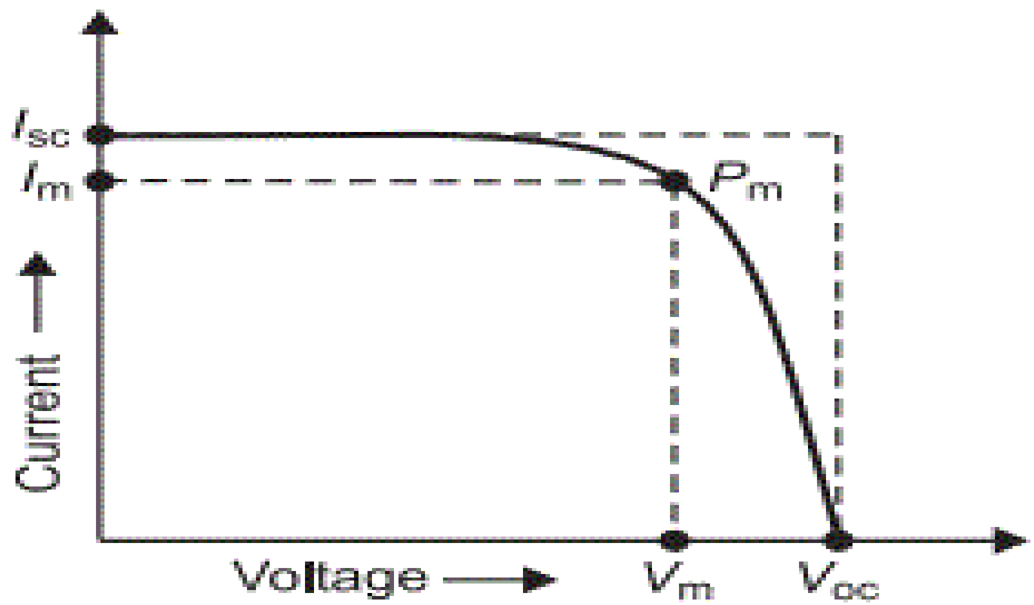

Figure 2. 2 I-V characteristics of solar cells [15].

for maximum power delivered to load we should write d_p/d_v= 0 by solving,

$$1 + \frac{I_L}{\mathrm{I(0)}} = \exp\left(\frac{\mathrm{e.Vm}}{kT}\right).\left[1+\frac{\mathrm{e.Vm}}{kT}\right] \qquad (2.9)$$

As shown in Figure 2.2, Vm is the voltage which produces maximum power, the maximum value of current I_m can be find if we substitute the value of exp ($\frac{\mathrm{e.Vm}}{kT}$) in all equations.

The maximum power is obtained by multiplying Vm and Im so,

$$P_m = \mathrm{Vm}.\frac{\mathrm{e.Vm}\,[I_L+\mathrm{I(0)}]/\mathrm{kT}}{1+\mathrm{e.Vm/kT}} \qquad (2.10)$$

Ratio of output power to incident optical power is defined as the conversion efficiency of solar cell. For maximum power output,

$$\eta\,\% = \frac{P_m}{P_{in}} \times 100 \qquad (2.11)$$

$$\eta\,\% = \frac{Vm.Im}{I.A} \times 100 \qquad (2.12)$$

Where, P_m is maximum power,P_{in} is input power V_m is maximum voltage, I_m is maximum current, I solar intensity (watt/ m^2), A area (m^2)

Fill Factor (FF) is the ratio of maximum power to the product of V_{oc} and I_{sc} [15]

$$\mathrm{FF}= \frac{V_m I_m}{V_{oc} I_{sc}} \qquad (2.13)$$

2.1.4 Types of Solar cells

Over the years, the researcher have tried to find a new solar cell based on different material and improve the efficiency of various solar cell technologies. When we classify the solar cells by the years there are three generations of solar cells as shown in Figure 2.3 along with their efficiencies in Table 2.1. Monocrystalline and polycrystalline belong to the first generation type of solar cells. Amorphous silicon, cadmium telluride and copper indium gallium selenide are the second generation types of solar cells. Third generation types of solar cells consist of solar cells which are recent solar cells and their research and development still continue in laboratories. These are copper zinc tin sulfide, dye-sensitized, organic perovskite and quantum dots solar cells. Here we briefly present a few solar cell technologies and describe the challenges confronted [17].

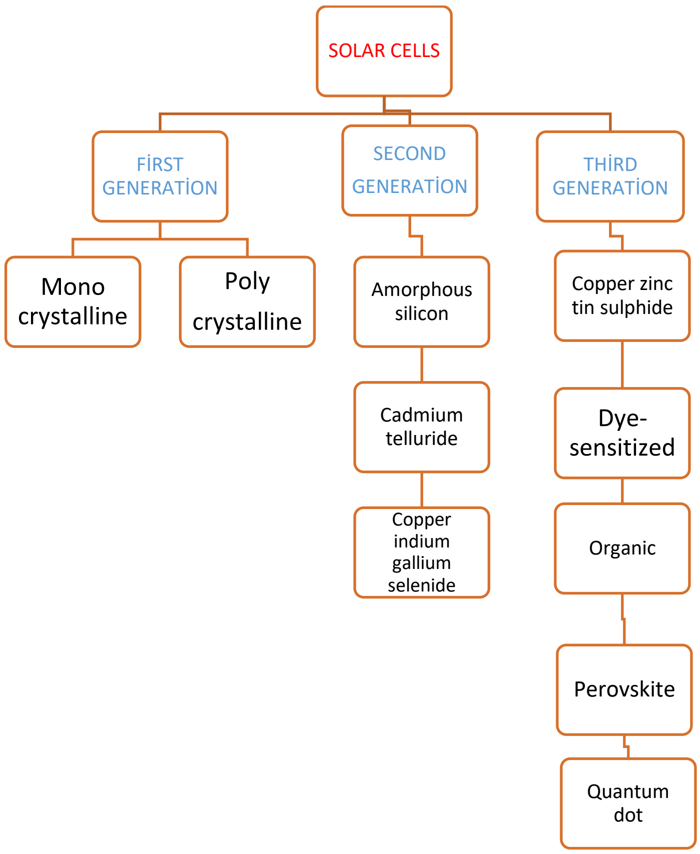

Figure 2.3 Classifications of solar cells.

2.1.4.1 Monocrystalline Solar Cells

Simple light harvesting properties are already utilized in commercial cells. Multilayer antireflection coatings and a surface texturization make easy to provide light scattering. Due to their high costs, people have looked into the possibility of not relying on expensive monocrystalline wafers. Si, GaAs or other III-V materials are used for monocrystalline solar cells. Because of nearly 200 µm wafer used for typical commercial Si monocrystalline cells, it has a high cost.

2.1.4.2 Polycrystalline Solar Cells

Polycrystalline solar cell wafer is based though not monocrystalline so it is cheaper than monocrystalline solar cells. The size of a polycrystalline solar cell typically in the mm range and it has a thickness less than 200 µm. Since it is cheaper than monocrystalline solar cells, it has a significant role in the photovoltaic markets. Optical optimization may be manipulated but is usually not considered because of the high cost.

Figure 2.4 Monocrystalline and polycrystalline silicon solar cells, respectively [47].

2.1.4.3 Amorphous Silicon

Silicon and germanium based solar cells are also another important member of this type of solar cells. Amorphous solar cells can be combined with microcrystalline Si solar cells. The thickness of these cells is typically 200 nm, but can be increased to 500 nm for several reasons related to the electrical characteristics.

2.1.4.4 Cadmium Telluride

The thickness of cadmium telluride solar cells is typically 5-10 μm. These cells require only minimal optical sophistication due to strong absorption in these materials. Researchers not considered on their photonic sophistication because it performs quite well. They consider decreasing the cost of solar cells. One of the results for the development of this type of solar cells is a new class of solar cells with a thin thickness less than 10 μm.

2.1.4.5 Copper Indium Gallium Selenide

These cells require only minimal optical sophistication due to strong absorption in these materials. Researchers not considered on their photonic sophistication because it performs quite well. The thickness of the copper indium gallium selenide solar cells is typically 2 μm with grain size on the order of 1μm.

2.1.4.6 Dye-sensitized Solar Cells

Dye-sensitized solar cells typically utilize extremely thin dye layers which act as an active layer that is coated on a random or rough nanostructured conducting surface, which provides for the charge separation and light trapping effect.

2.1.4.7 Organic Polymer Solar Cells

The main function of organic polymer solar cells is to address the fact that photon absorption leads to exciton instead of free carrier generation. This type of solar cells are often narrowband absorbers and they are typically found in a bulk heterojunction structure with two different materials mixed in the active bulk excitons. Typically, they have a very limited diffusion length and require a heterojunction in order to dissociate [18].

Classification (type)	Efficiency (%)	Area (cm^2)	Voc (V)	Isc (A)	FF (%)	Test Centre	Date	Description
Si (crystalline)	24.4± 0.5	13177 (da)	79.5	5.04	80.1	AIST	(9/16)	Kaneka (108 cells)
multicrystalline	19.9 ±0.4	15143 (ap)	78.87	4.795	79.5	FhG-ISE	(10/16)	Trina solar (120 cells)
GaAs (thin film)	25.1 ± 0.8	866.45 (ap)	11.08	2.303	85.3	NREL	(11/17)	Alta devices46
CIGS (Cd free)	) 19.2 ± 0.5	841 (ap)	48.0	0.456	73.7	AIST	(1/17	Solar frontier (70 cells)
CdTe (thin-film	18.6 ±0.5	7038.8 (da)	110.6	1.533	74.2	NREL	(4/15)	First solar, monolithic
a-Si/nc-Si (tandem)	12.3 ± 0.3	14322 (t)	280.1	0.902	69.9	ESTI	(9/14)	TEL solar, Trubbach labs
Perovskite	11.6 ± 0.4	802 (da)	23.79	0.577	68.0	AIST	(4/18)	Toshiba (22 cells)
Organic	8.7 ± 0.3	802 (da)	17.47	0.569	70.4	AIST	(5/14	Toshiba
InGaP/GaAs/InGaAs	31.2 ± 1.2	968 (da)	23.95	1.506	83.6	AIST	(2/16)	Sharp (32 cells)
CIGS (large)	15.7 ± 0.5	9703 (ap)	28.24	7.254	72.5	NREL	(11/10)	Miasole

Table 2. 1 Efficiency table of solar cells under the global AM 1.5 spectrum (1000 W/m^2) at a cell temperature of 25° [19].

2.2 Metamaterials

Metamaterials (MMs) are a new concept of interdisciplinary research which is related to artificial material for displaying physical properties not available in nature. Firstly, they were proposed for tailoring electromagnetic of media and optical properties, then they have been started to be use for elastic, acoustic, and thermal properties. Since 1999, metamaterials have taken enormous attention from the scientific community and use in the field of the antenna, waveguide engineering, imaging, microscopy, sensing and light manipulation [21].

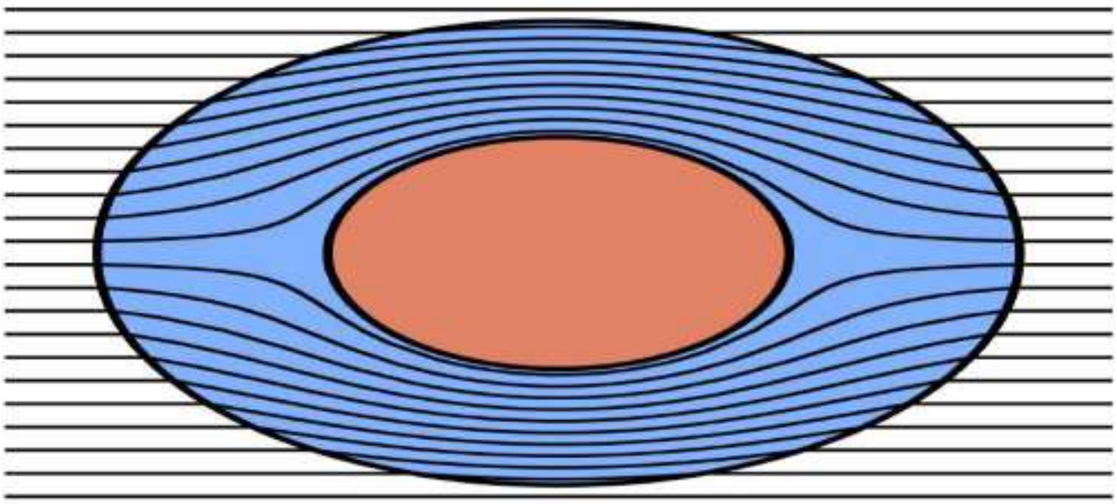

Figure 2.5 Electromagnetic metamaterials [21].

2.2.1 Classification of Metamaterials

According to continuous media theorem, electromagnetic properties of the materials determined by parameters of permittivity ε and permeability μ. Metamaterials are classified into four groups on the basis of permittivity ε and permeability μ as shown in figure 2.6.

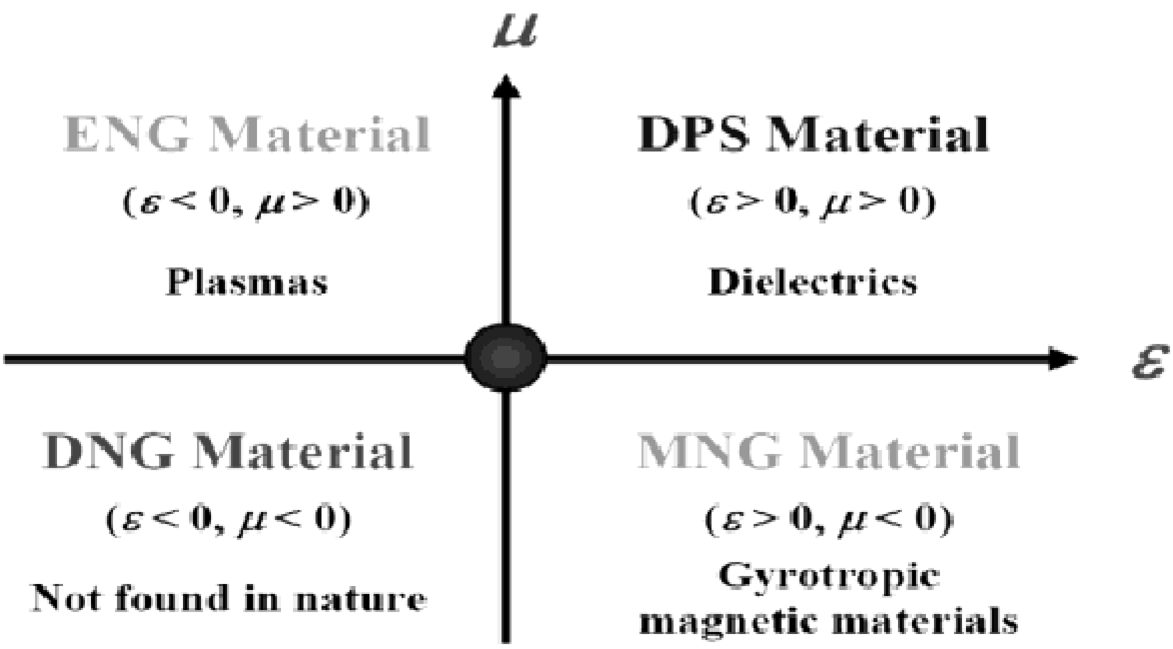

Figure 2.6 Classification of metamaterials [22].

2.2.1.1 Double Positive Materials

Double positive materials (DPS) which have both permittivity and permeability greater than zero ($\varepsilon > 0$, $\mu > 0$). Dielectric media fall under this category.

2.2.1.2 Epsilon Negative Materials

A plasma environment carries this characteristic in a certain frequency spectrum. Epsilon negative materials (ENG) have permittivity less than zero and permeability greater than zero ($\varepsilon < 0$, $\mu > 0$).

2.2.1.3 Mu Negative Materials

Some gyrotropic materials present this characteristic in a certain frequency spectrum. Mu negative materials (MNG) have permittivity greater than zero and permeability less than zero ($\varepsilon > 0$, $\mu < 0$).

2.2.1.4 Double Negative Materials

The member of this type of materials can only be produced artificially. A double negative material (DNG) has both permittivity and permeability less than zero ($\varepsilon < 0$, $\mu < 0$).

2.2.2 Types of Metamaterials

2.2.2.1 Electromagnetic Metamaterials

Electromagnetic MMs are used for microwave and optical applications which have a new subject within electromagnetism and physics. Microwave couplers**,** beam steerers, antenna radomes, band-pass filters and lenses are some applications of the electromagnetic metamaterials.

2.2.2.1.1 Single Negative Metamaterials

Single negative materials (SNG) have negative permittivity or permeability. Due to their dispersive nature with the change in frequency, single negative materials can change their parameters such as refractive index n, permittivity ε and permeability μ.

2.2.2.1.2 Double Negative Metamaterials

These MMs (negative refraction index or backward wave media) have both negative permittivity and permeability with negative refraction index.

2.2.2.1.3 Electromagnetic Band Gap Metamaterials

Electromagnetic bandgap metamaterials have a function that can control and manipulate the propagation of electromagnetic waves which have artificial structure.

2.2.2.1.4 Bi-isotropic and Bi-anisotropic Metamaterials

This types of metamaterials is described by the permittivity and permeability parameters based on the independent electric and magnetic responses which are categorized into the single or double negative metamaterials. In some samples of electromagnetic metamaterials, electric field creates magnetic polarization and magnetic field induces an electrical polarization like magneto-electric coupling. These media are known as bi-isotropic media because it present magneto-electric coupling and if it is anisotropic, it is called as bi-anisotropic [22].

2.2.2.2 Chiral Metamaterials

Series of dielectric gammadion or planar metallic on a substrate can be chiral metamaterials. When light is coming through the series linearly, it transforms elliptically polarized on coaction by the gammadions with the same way as the gammadion itself [22].

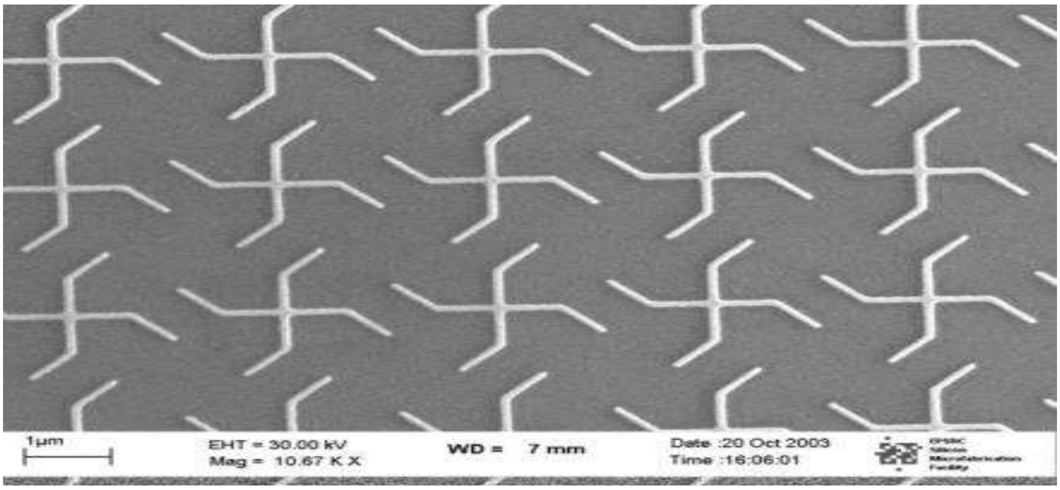

Figure 2.7 Chiral metamaterials [22].

2.2.2.3 Terahertz Metamaterials

Combining of artificial materials which interact at terahertz (THz) frequencies and still in research process known as terahertz metamaterials. They are passive materials that have negative permeability can achieve a desired magnetic response. Terahertz waves starts with microwave band and end with an infra-red band [22]

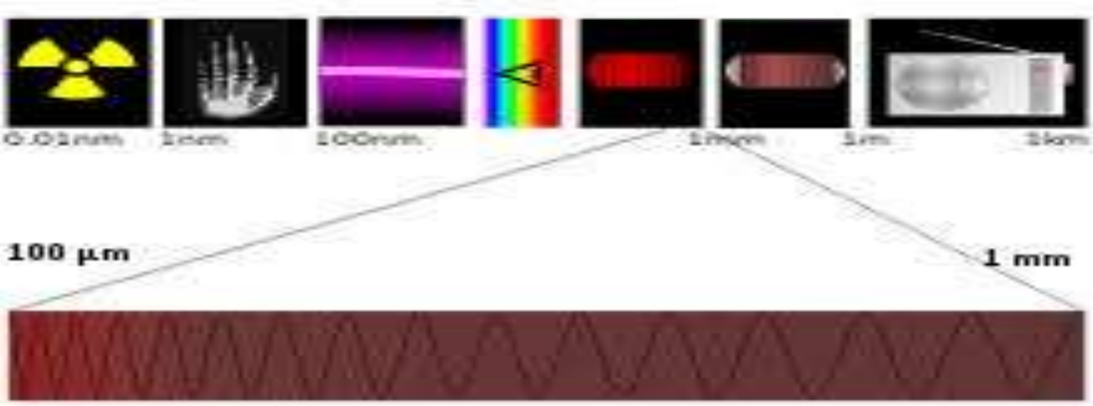

Figure 2. 8 Wave formation of Terahertz metamaterials [22].

2.2.2.4 Photonic Metamaterials

One of the other electromagnetic materials is a photonic material that used to interact with optical frequencies. They radiate the source at optical wavelengths. Also, the period of subwavelength separates photonics metamaterials from photonic bandgap structure. This is because optical properties originate sub-wavelength interaction with the light spectrum do not from photonic band gaps. Photonic metamaterials have large research area with capability of zero indexes of refraction and negative values for index of refraction [22].

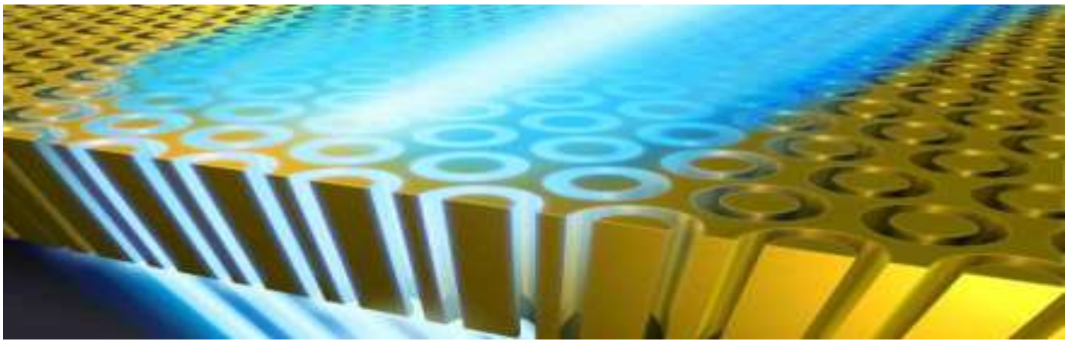

Figure 2.9 Photonic Metamaterials [22].

2.2.2.5 Tunable Metamaterials

Changing the frequency of the refractive index is the main properties of the tunable metamaterials. An incident electromagnetic wave can manipulate with these metamaterials. They can be arranged from index of negative values to zero or positive values. Due to changeable the permittivity of liquid crystal, tuning in the near infrared range is reached. Also, negative values can be increased or decreased [22].

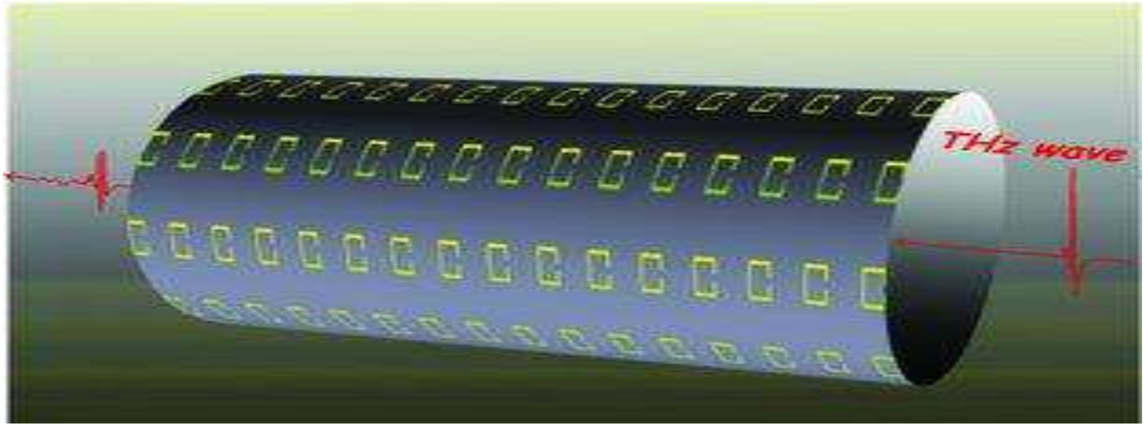

Figure 2.10 Tunable Metamaterials [22].

2.2.2.6 Frequency Selective Surface Based Metamaterials

Frequency selective surface based metamaterials can alter the frequencies in a single medium however impossible to change in stable frequency response. This types of metamaterial is first developed materials that can control the transmission and reflection behaviour of an incident radiation wave. Particular geometrical shapes of frequency selective surface based metamaterial can be fabricated as periodic series by elements of two dimensional planar [22].

2.2.2.7 Nonlinear Metamaterials

Nonlinear metamaterials are artificial materials that can be made by some kind of metamaterials that have properties to change the power of the incident wave. The electromagnetic response of this type metamaterials described with permeability and permittivity. Also, they are artificial materials in which the nonlinearity appear because microscopic electric field of the inclusions greater than macroscopic electric field of the electromagnetic source [22].

2.2.3 Applications of Metamaterial

There are many application fields of metamaterial including solar power management, high-frequency field communication, improving ultrasonic sensors, public safety, sensor detection high gain antennas, remote aerospace, public safety, and sensor detection applications. In this part, we will give some examples of applications of metamaterials [22].

2.2.3.1 Detectors

Detectors have used in many applications like cargo and screening passenger, biological agent, contamination, detection of the presence of chemical explosives.

2.2.3.2 Revolutionary Electronics

Due to future circuits made with the use of light rather than electricity, army engineers use the metamaterials as a switching device for building fast and small photonic equipment. Harvesting of light can be turned on and turned off a combination of metamaterials and semiconductor in the device [22].

2.2.3.3 Light and Sound Filters

Nano scale wrinkles of metamaterials are used to control light and sound that increase ultrasound resolution and to change the color of the material. Selected frequencies created by compressing materials scatter by the precise wrinkles spacing. These are used in nondestructive material testing, sound suppression, medical diagnostics. Light and sound filtering can be made with high precision and multilayer deposition. Control of each thickness of layer is possible by using a fraction of wavelength [22].

2.2.3.4 Biosensors

Using the biosensor in the areas of food safety, disease diagnostics, environmental monitoring shows that they are very important tools. The researcher used this type of metamaterials in terms of fluorescence based methods because of biosensor have high ability of detection of label free biomolecules and efficient cost than fluorescence based methods [22].

2.2.3.5 Metamaterial Absorbers

Metamaterial absorber absorbs electromagnetic radiation. Supplementary miniaturization, wider adaptability, and increased effectiveness are the benefits over the conventional absorbers. Effective medium design, permittivity, and permeability are the requirements for the generate a high ratio of electromagnetic radiation absorption [22].

2.2.3.6 Metamaterial Antennas

Metamaterials antennas increase the performance of the miniaturized antenna systems which has a original band gap properties and periodic structures. This structure increases the gain of an antenna. On the contrary of small conventional antennas, metamaterials antenna has a structure that can store and re-radiate energy which makes its size small and behaves like a larger antenna [22].

2.3 Two-Dimensional (2D) Materials

The space we are in is three-dimensional. Solids, liquids and gases formed by the combination of atoms occupy a volume in this space. One of the active research areas of today is two-dimensional materials, also known as single-layer materials. The structure of these materials is similar to that of crystalline solids. However, like ordinary crystalline solids, they are not three-dimensional, but two-dimensional. In crystalline solids, atoms form a three-dimensional and regular structure that occupies a volume in space. The material is multi-layered and there are strong or weak bonds between the different layers. For example, graphite and diamond as shown in Figure 2.11 and Figure 2.12, respectively formed by the combination of carbon atoms are examples of three-dimensional crystalline solids. Carbon atoms in graphite with a very soft structure are connected to each other in layers to form hexagons. The softness of the material is due to the weak bonding between the different layers [42].

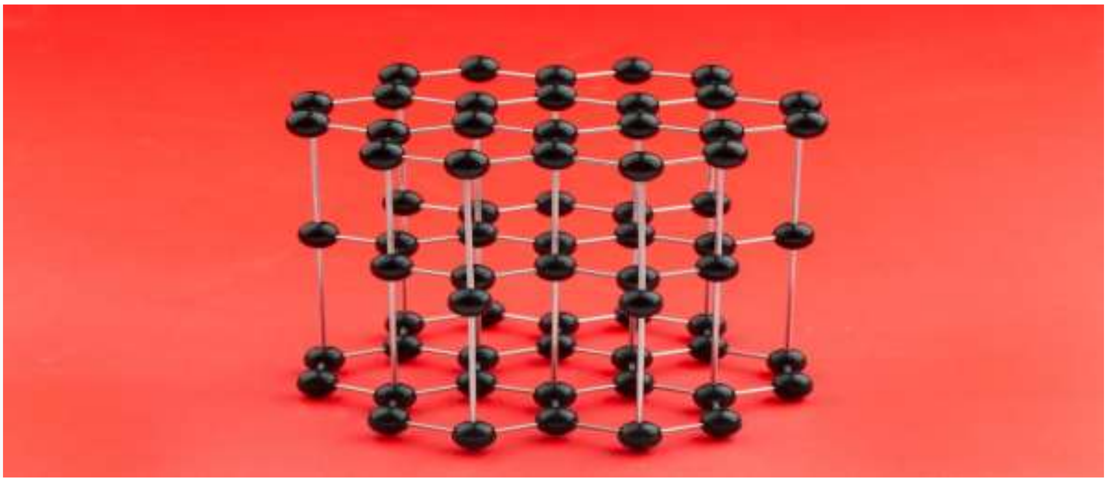

Figure 2. 11 Atomic structure of graphite [42].

Diamond, which is one of the hardest materials in nature, builds strong bonds with its four closest neighbors, located in layers above and below carbon atoms in a layer. The first sample of monolayer materials obtained in the laboratory was graphene as shown in Figure 2.13. Andre Geim and Konstantin Novoselov used a sticky tape to remove a layer of graphite in 2004 and then transfer it onto a silicon plate [42].

Figure 2. 12 Atomic structure of diamond [42].

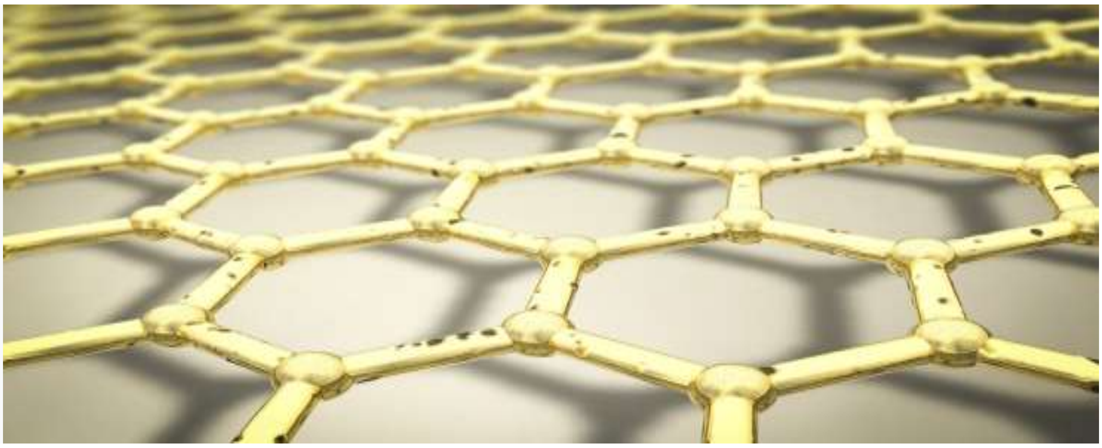

Figure 2.13 Atomic structure of graphene [42].

Graphene, carbon nanotube, MXene (2D carbides/nitrides), transition metal dichalcogenides are well known types of 2D material. Transition metal dichalcogenides include molybdenum disulfide (mos_2), molybdenum diselenide ($mose_2$), tungten diselenide (wse_2), hexagonal boron nitride (h-BN), borophene (2D boron), silicene (2D silicon), germanene (2D germanium) [42].

2D materials offers many promising properties compared to traditional photonic material such as gallium arsenide and silicon. Firstly, surface of 2D material naturally passivated without any bond. It means that integration of 2D materials with photonic structures is possible [42]. Many 2D materials have ability to interact with light strongly despite being atomically thin. Also 2D materials have diverse electronic properties that can cover wide electromagnetic spectrum [43].

Ability of strong interaction with photon in a broad energy range encourage the researchers to investigate graphene for photodetection applications. Also graphene has high carrier mobility to be candidate for high speed applications in a wide frequency region [44].

2.3.1 Carbon Nanotube

Carbon is the chemical element and has six electrons in its orbital with atomic number 6. It has ability to hybridize in sp, sp^2, or sp^3 forms to produce constant nanometer sp^2 carbon bonded materials such as carbon nanotube, fullerenes and graphene [27].

Carbon nanotubes take most of the physical properties from graphene. Carbon atoms regularly organized with sp^2 connected atomic scale hexagonal model in graphene. Hexagonal model is also basic structure model for carbon nanotubes and fullerenes whichs are allotropes of graphene [28].

Carbon nanotube is a cylinder made of rolled graphene sheet and theorically different as shape from graphene. Single walled carbon nanotube and multi walled carbon nanotube are types of carbon nanotube as shown in Figure 2.14 and Figure 2.15, respectively. Nanotubes with single wall was reported in 1993 as first time while the ones more than one wall are multiwall carbon nanotube were first discovered in 1991 by Lijima [28].

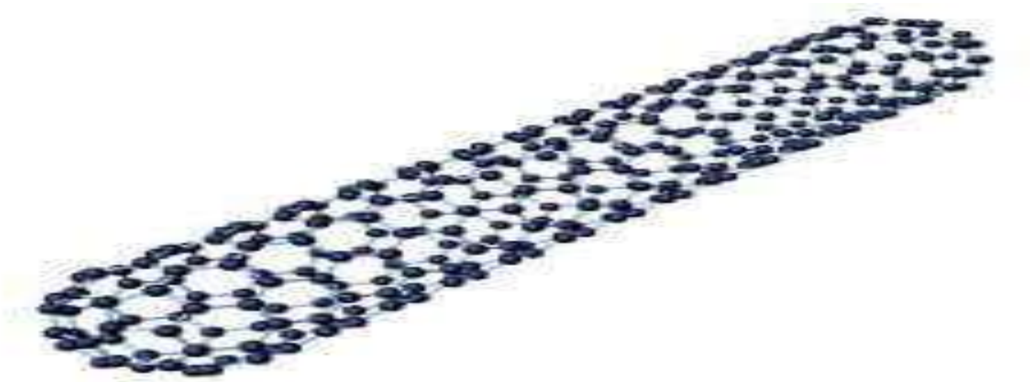

Figure 2.14 Single walled carbon nanotube molecular structure [29].

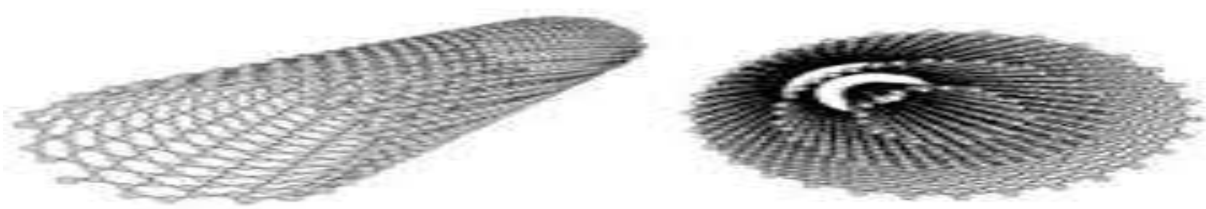

Figure 2.15 Multi walled carbon nanotube molecular structure [29].

There are three different forms of SWCNTs depend on wrapping to a cylinder path such as armchair, chiral, and zigzag shown in Figure 2.17. The structure of SWCNT is characterized by a pair of indices (n,m) that known as chiral vector that can directly effect on electrical properties of nanotubes.The integer n and m represent directions of graphene in honeycomb crystal lattice. Well known opinion, if m=0 the name of nanotube is zigzag, when n=m, nanotubes called armchair and in other stuations called chiral [29].

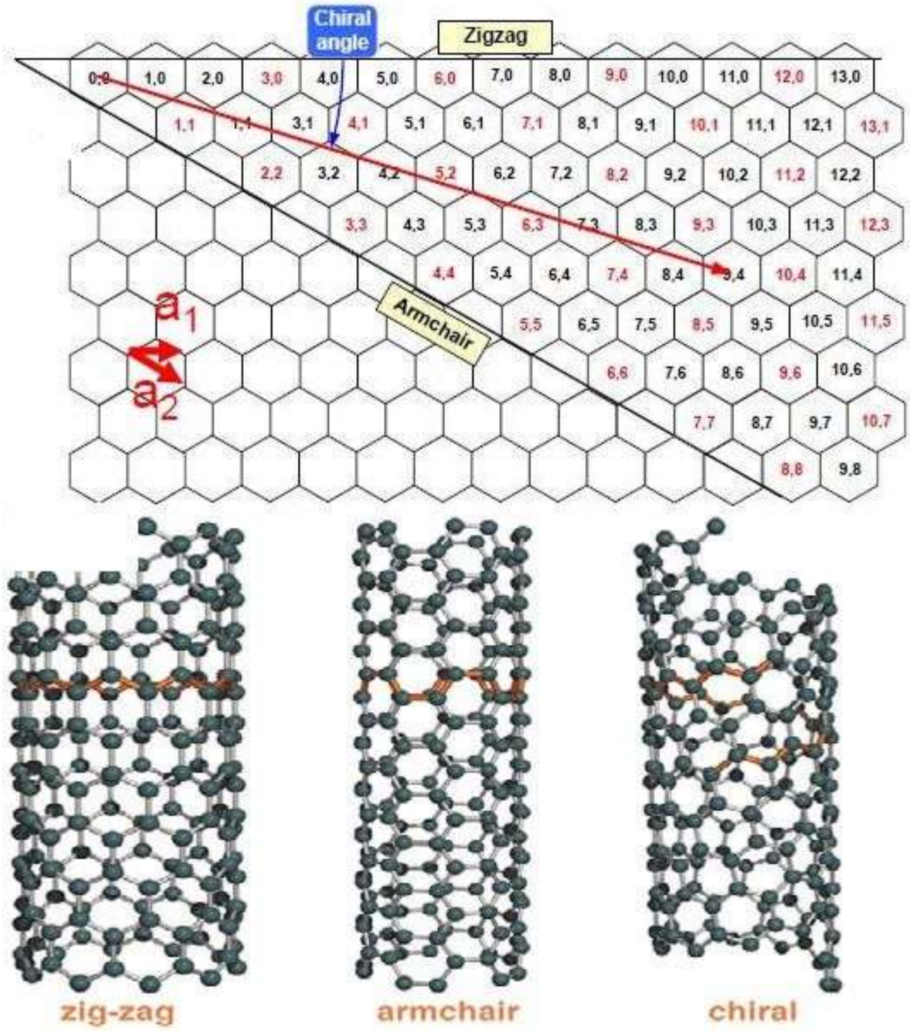

Figure 2.16 Different forms of single walled nanotubes [29].

Carbon nanotube has promising properties such as $1/12.9\,kW^{-1}$ thermal conductance, 1.40 g/cm^3 density, 10^{-4}W /cm at 300 K resistivity, 10^7 A / cm^2 conductivity. This properties take reseracher attentions, and so applied in energy storage and medical applications.[30]

2.3.2 MXene

Two dimensional materials like graphene and TMDs have unique properties as mentioned before. MXene is a new member of 2D materials family with wide range of chemistries offering the way for better understanding of differences between properties of 2D and 3D structure, lead to description of useful properties of 2D nitrides, carbides, oxycarbides and end up with new applications.

The basic structure of MXene is MAX phase which have been researched for years and many samples of carbides, nitrides and carbonnitrides have been synthesized with various properties. Discovery of Mxene date back to 2011 when a research team from Drexel university they removed unwanted layers of aliminum from layers of titanium carbide by applying etchant of fluoride salt and hydrochloric acid on bulk MAX phase. General Formula that determine name of mxene $is\ M_{n+1}AX_n$, where n=1, 2, 3, M states a transition metal, A is an element such as aluminum or silicon and X is carbon and nitrogen. MXenes exhibit an unusual, unique, combination of properties. For example they are elastically stiff, strong, brittle and heat tolerant like ceramics, while they conduct heat and electricity like metals. Sometimes they are resistant to chemical attack, thermal shock, damage, tolerant and sometimes creep, fatique and oxidation resistant [31].

Figure 2.17 Scanning electron micrograph of MXene particle.

Figure 2.17 Scanning electron micrograph of MXene particle.Thanks to this properties of MXene, researcher focus on the investigation of MXene in different applications such as thermoelectricity [32], superconductivity [33], photocatalysis [34], ion batteries [35], gas sensors [36] and hydrogen storage [37].

2.3.3 Photovoltaic Applications of MXene

The aim of this part is to mention about publications related to photovoltaic applications that use MXene materials. As we mentioned before, since MXene is a new member of 2D materials family discovered in 2011, the study or publications about MXene is not too much.

Kang et al. studied the optoelectronic properties of $Ti_3C_2T_x$ with n-type silicon of vertical Van der Waals heterostructures. Investigation of temprature and ilumination, applied voltage on $Ti_3C_2T_x$ / n-si schottky junction heterostructure shows that MXene has excellent photoelectric properties to use in the photoelectrical field [38].

Chaudhuri et al. fabricated plasmonic absorbers using a MXene film that has strong localized surface plasmonic resonances and achieved nearly % 90 absorption [39].

Guo et al. studied on integration MXene film with the perovskite absorber layer for efficiency enhancement of perovskite solar cells. Device performance is achieved %12 enhancement by 0.003 wt% amount of MXene additive, after optimizing key parametrs. Also solar cell parameters analyzed after additive of MXene [11].

Yang et al. used MXene nanosheets as a conductive additive in the SnO_2 to prepare SnO_2-mxene electron transport layers for perovskite solar cells. Proper addition mxene to SnO_2 layer can increased the conductivity, which is beneficial for higher short circuit current density (Jsc) and fill factor (FF) values [40].

2.4 Basics of TE, TM and TEM Modes

The electrical and magnetic field lines are always perpendicular to each other and they travel in the waveguide as electromagnetic waves [23]. The simplest waveform in the waveguide is shown in Figure 2.18.

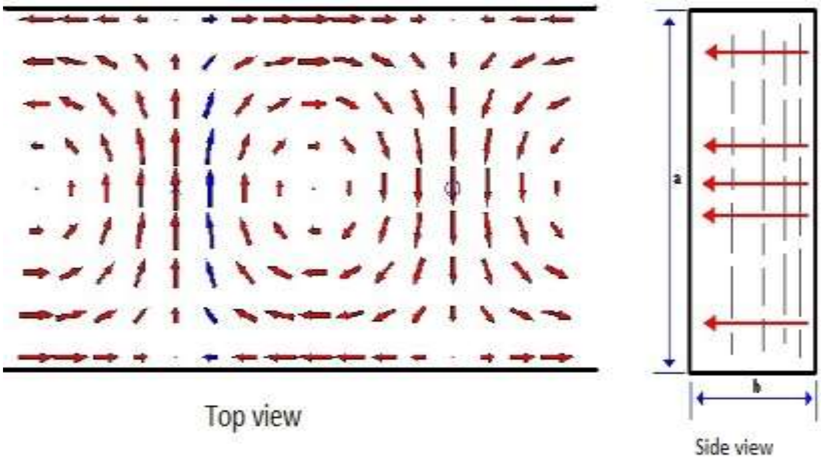

Figure 2.18 The most common electromagnetic waveform in a rectangular waveguide.

The straight lines in Figure 2.18 are voltage lines and E indicates the direction of the electric field. The dashed lines indicate the magnetic field H. These field lines are field lines at one time and change their form over time. As can be seen from the cross-sectional view of the guide in the Figure 2.18, there is a voltage parallel to the upper and lower faces, i.e, between the major faces, and has the largest value in the center. On the side face, the voltage is short circuited and the electrical field is zero along these edges. A waveguide usually consists of two waveforms.

First, the electrical field is perpendicular to the direction of propagation as shown in Figure 2.18. This waveform called Transverse Electric (TE), in the second type waveform, the magnetic field lines are perpendicular to the direction of propagation, as shown in Figure 2.19 and Figure 2.20 which is called Transverse Magnetic (TM). In other words, there is no projection of electrical field lines in the direction of propagation in TE form waves [23].

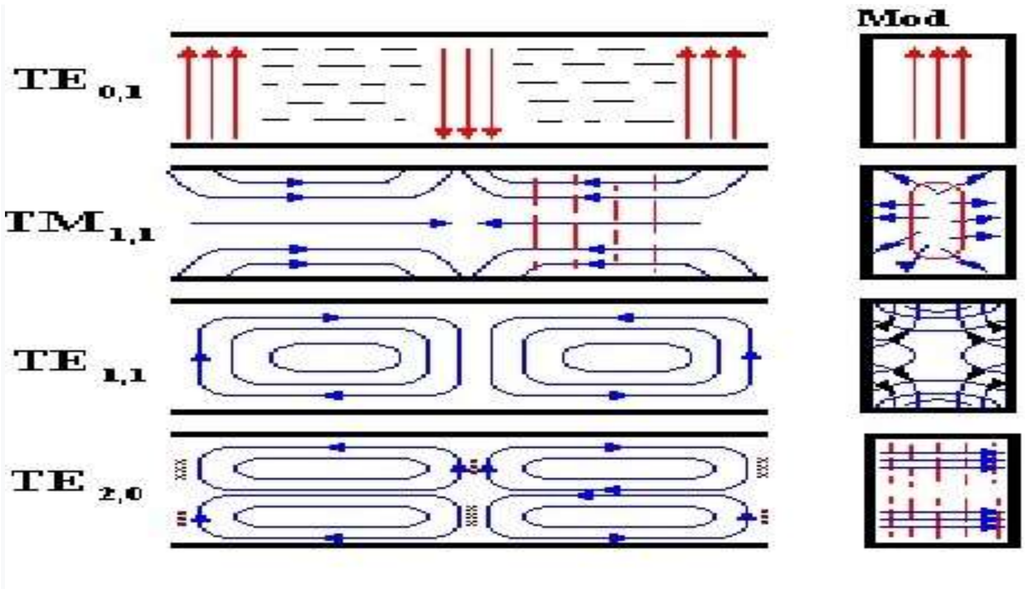

Figure 2.19 Representation of modes in rectangular waveguide.

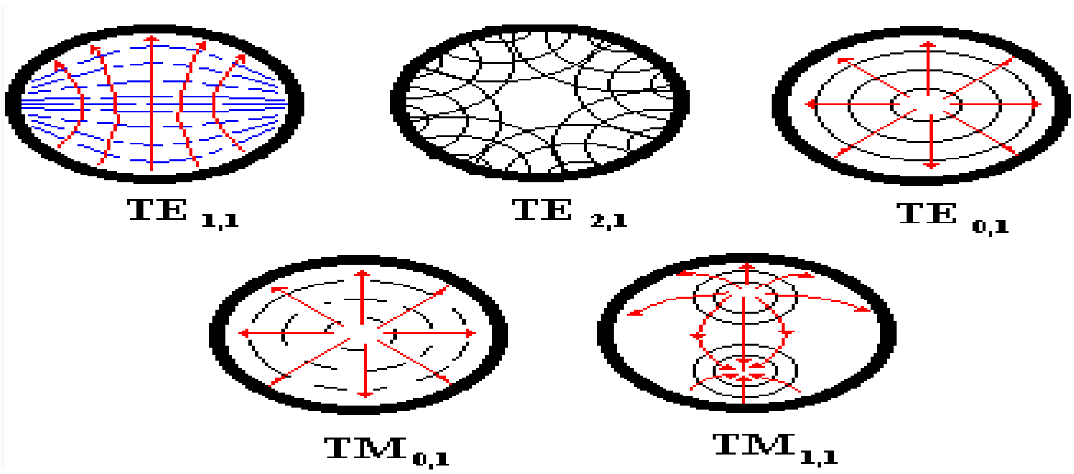

Figure 2.20 Representation of modes in circular cross-section waveguide

In order to describe a particular shape in TE or TM waves, two sub-digits indicating the change of the electric field are placed. The first shows the number of half wave changes on the wide edge of the electric field and the second shows the number of wave changes on the narrow side of the electric field. If we examine the waveform of Figure 2.18, on the wide edge, the electric field starts at zero at the end and becomes maximum when it reaches center. It becomes zero again when it reaches other edge. That is, the electric field varies by a half wave along the wide edge. On the narrow side, the number of voltage changes is zero because the voltage is zero across the entire edge. Accordingly, this wave is a $TE_{1,0}$ waveform. Figure 2.19 shows that cross-sectional and longitudinal cross-sectional views of four different waveforms [23].

The propagation where the electric and magnetic field lines are all limited to directions normal to the direction of propagation is called Transverse electromagnetic (TEM) mode. Transverse electromagnetic mode is characterized by $E_Z = H_Z = 0$

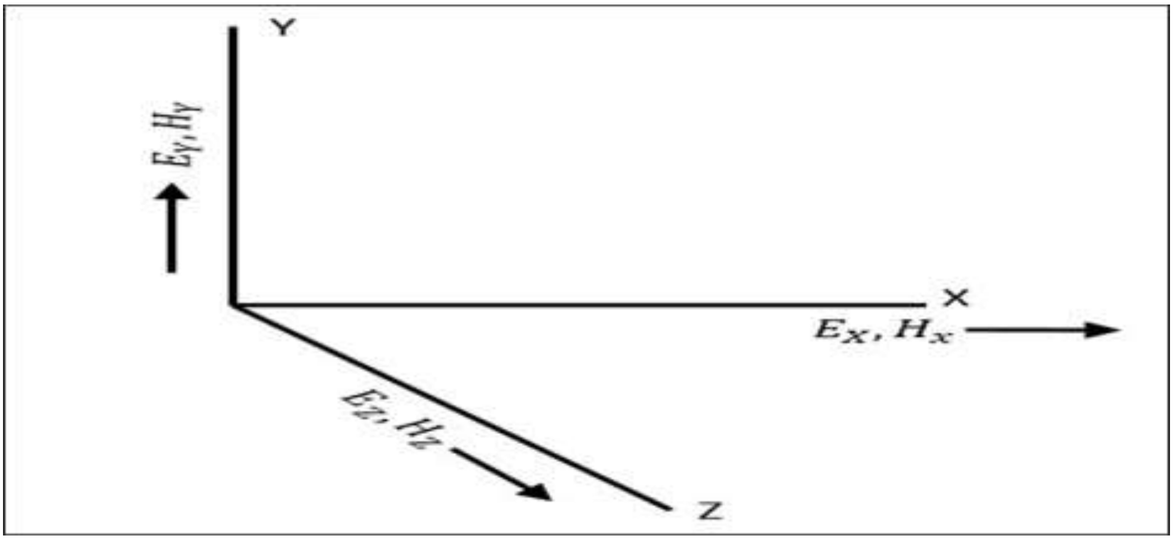

Figure 2.21 Directions of propagation [24].

$$H_x = \frac{j}{k_c^2} \left(\omega\varepsilon \frac{\partial E_z}{\partial y} - \beta \frac{\partial H_z}{\partial x} \right) \quad (2.14)$$

$$H_y = - \frac{j}{k_c^2} \left(\omega\varepsilon \frac{\partial E_z}{\partial x} + \beta \frac{\partial H_z}{\partial y} \right) \quad (2.15)$$

$$E_x = - \frac{j}{k_c^2} \left(\beta \frac{\partial E_z}{\partial x} + \mu\omega \frac{\partial H_z}{\partial y} \right) \quad (2.16)$$

$$E_y = \frac{j}{k_c^2} \left(-\beta \frac{\partial E_z}{\partial y} + \mu\omega \frac{\partial H_z}{\partial x} \right) \quad (2.17)$$

When we apply the $E_Z = H_Z = 0$ condition we will obtain equations shown in below,

$$\frac{\partial E_z}{\partial y} + j\beta E_y = -j\omega\mu H_x \tag{2.18}$$

$$-j\beta H_x - \frac{\partial H_z}{\partial x} = j\omega\varepsilon E_y \tag{2.19}$$

$$\beta^2 E_y = \omega^2 \mu\varepsilon E_y \tag{2.20}$$

$$\beta = \omega\sqrt{\mu\varepsilon} = k \tag{2.21}$$

The cutt of wave number

$$k_c = \sqrt{k^2 - \beta^2} = 0 \tag{2.22}$$

for TEM waves [24].

2.4.1 Cut-off Wavelenght and Cut-off Frequency

The waveguides have a wavelength cut-off values for each waveform. This value is defined by $\lambda c = 2a$. For example, for a rectangular waveguide, the $TE_{1,0}$ waveform is $\lambda c = 2a$. Where a is the wide edge of the rectangle, b is the narrow edge as shown in Figure 2.19**.** At frequencies greater than 2a wavelength, there may be no transmission in the waveguide. λ_c is briefly referred to cut-off wavelength and it is possible to use same term for frequency as cut-off frequency. Table 2.2 shows the cut-off wavelengths for several commonly used waveforms. A careful examination of Table 2.2 shows that $TE_{1,0}$ is the waveform with the largest cut-off wavelength [25].

Types of Wave (mode)	λ_c
$TE_{1,0}$	2a
$TM_{1,1}$ or $TM_{1,1}$	$\frac{2ab}{\sqrt{a^2+b^2}}$
$TE_{2,0}$	a
$TE_{0,1}$	2b
$TE_{m,n}$ or $TM_{m,n}$	$\frac{2}{\sqrt{\left(\frac{m}{a}\right)^2+\left(\frac{n}{b}\right)^2}}$

Table 2.2 Cut-off wavelenghts in rectangular waveguide [25].

If two or more waves pass through a waveguide at the same time, they may interfere unintentionally. Therefore, only a dominant form is required in a waveguide. Any point of absence in the grid may also produce contradictory forms, but these are often sub-cut and will soon fade away [25].

For waveguides with circular cross-sections, as with rectangles, each waveform has a definition of cut wavelength. In this definition, the cut-off wavelenght value is given as a function of the inner diameter d of the guide tube. Table 2.3 shows the cut wavelengths for some of the most common waveforms in circular cross-section waveguides. It can be seen from the Table 2.3 that the form of $TE_{1,1}$ is the dominant form.

Types of Wave (mode)	λ_c
$TE_{1,1}$	1,706d
$TM_{0,1}$	1,306d
$TE_{2,1}$	1,028d
$TE_{0,1}$	0820d
$TM_{1,1}$	0820d

Table 2.3 Cut-off wavelengths in circular waveguide [25].

2.4.2 Wavelength in Guide

Wavelengths in a waveguide and in the air have different values. The equation (2.22) gives the connection between the wavelength in guide, cut-off wavelength of any wave.

$$\frac{1}{\lambda_g{}^2} = \frac{1}{\lambda_0{}^2} - \frac{1}{\lambda_c{}^2} \qquad (2.23)$$

Here λg gives the wavelength in guides, $\lambda 0$ wavelength in gap , λc gives the cut-off wavelength. From the equation (2.22) we can solve the λg,

$$\lambda_g = \frac{\lambda_0}{\sqrt{1-\left(\frac{\lambda_0}{\lambda_c}\right)^2}} \qquad (2.24)$$

This equality is true for any wave that is transmitted in any waveguide, λ_c must be the correct value for the given waveform and guide section. If we examine the equation (2.23) carefully, when λ_e is too small relative to λ_c, it remains only 1 in the denominator, which is the guide wavelength equal to the gap wavelength. If value of λ_0 approaches λ_c, then λ_g will increase. If λ_0 is equal to λ_c, $\lambda_g$is infinite. Finally, if λ_0 is greater than λ_c, λ_g will be the imaginary number [25].

2.4.3 Solution for TE, TM and TEM Modes

A wave travels through a waveguide (dielectric)

$$\text{E(x, y, z)}=E^0\text{(x,y)}e^{-\gamma z} \qquad (2.25)$$

$$\text{H(x, y, z)}=H^0\text{(x,y)}\, e^{-\gamma z} \qquad (2.26)$$

Ampere and Faraday laws for a source-free region are shown in equation (2.26) and (2.27)

$$\nabla\times H = j\omega\epsilon E \tag{2.27}$$

$$\nabla\times E = -j\omega\mu H \tag{2.28}$$

Equation (2.27) and (2.28) produces some equations for the x, y and z directions shown in equations below,

$$\frac{\partial Ez}{\partial y} + \gamma E_y = -\, j\omega\mu H_x \tag{2.29}$$

$$\frac{\partial E_z}{\partial x} + \gamma E_z = j\omega\mu H_y \tag{2.30}$$

$$\frac{\partial Ey}{\partial x} - \frac{\partial Ex}{\partial y} = -\, j\omega\mu H_z \tag{2.31}$$

$$\frac{\partial Hz}{\partial y} + \gamma H_y = j\omega\epsilon E_x \tag{2.32}$$

$$\frac{\partial Hz}{\partial y} + \gamma H_z = -\, j\omega\epsilon E_y \tag{2.33}$$

$$\frac{\partial H_y}{\partial x} - \frac{\partial Hz}{\partial y} = j\omega\epsilon E_z \tag{2.34}$$

$$H_x = -\,\frac{\gamma}{h^2}\frac{\partial H_z}{\partial x} + \frac{j\omega\varepsilon}{h^2}\frac{\partial E_z}{\partial y} \tag{2.35}$$

$$H_y = - \frac{\gamma}{h^2}\frac{\partial H_z}{\partial x} - \frac{j\omega\varepsilon}{h^2}\frac{\partial E_z}{\partial x} \quad (2.36)$$

$$E_x = - \frac{\gamma}{h^2}\frac{\partial E_z}{\partial x} - \frac{j\omega\mu}{h^2}\frac{\partial H_z}{\partial y} \quad (2.37)$$

$$Ex = \frac{\gamma}{h^2}\frac{\partial E_z}{\partial y} + \frac{j\omega\mu}{h^2}\frac{\partial H_z}{\partial x} \quad (2.38)$$

and

$$h^2 = \gamma^2 + \beta^2 \quad (2.39)$$

where

$$\beta = \omega\sqrt{\mu\varepsilon} \quad (2.40)$$

Ez =0, Hz ≠ 0 for TE mode, Ez≠0, Hz=0 for TM mode and Ez = Hz = 0 for TEM mode. Solve the partial differential for TE and TM modes we need Helmholz equation shown in equation (2.41),

$$\nabla^2 A + k^2 A = 0 \quad (2.41)$$

In TE mode we need H_z which is our A in the Helmholtz equation and our factor k^2 is β^2.Then,

$$\nabla^2 H_z + \beta^2 H_z = 0 \quad (2.42)$$

$$\frac{\partial^2}{\partial x^2}H_z + \frac{\partial^2}{\partial y^2}H_z + \frac{\partial^2}{\partial z^2}H_z + \beta^2 H_z = 0 \quad (2.43)$$

$$\frac{\partial^2}{\partial z^2}H_z = -\gamma^2 H_z^0\,(x, y)\, e^{-\gamma z} \quad (2.44)$$

$$\frac{\partial^2}{\partial x^2}H_z^0 + \frac{\partial^2}{\partial y^2}H_z^0 + (\gamma^2 + \beta^2)\, H_z \quad (2.45)$$

Since

$$h^2 = \gamma^2 + \beta^2 \quad (2.46)$$

$$\frac{\partial^2}{\partial x^2}H_z^0 + \frac{\partial^2}{\partial y^2}H_z^0 + h^2 H_z = 0 \quad (2.47)$$

Repeat the same steps for TM mode where we need E_z

$$\nabla^2 E_z + \beta^2 E_z = 0 \quad (2.48)$$

and therefore

$$\frac{\partial^2}{\partial x^2}E_z^0 + \frac{\partial^2}{\partial y^2}E_z^0 + h^2 E_z = 0 \quad (2.49)$$

2.5 Physics of Absorption for Solar Cells

Basically, when electromagnetic radiations reach the surface of solar cells, three diffrent parameters affect their efficiency. Some of radiations absorbed by the cell while others are reflected back, remain parts of radiation transmitted through the cells to the space. Scattering parameters which are the function of electric fields ease the understanding the physics behind absorption for high frequencies range [26].

2.5.1 Scattering Parameters (s-parameters)

The parameters related to electromagnetic Scattering are called S-parameters. These parameters are used for description of the reflection and transmission phenomena that occur due to the reflected and transmitted wave. Figure 2.23 shows the diagram for a two-port system. The left side of the system is named as port 1 while right side is named as port 2.

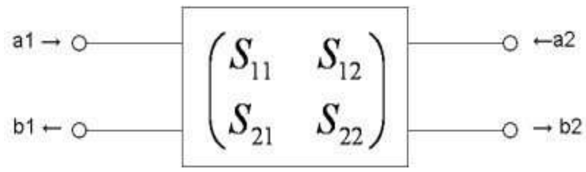

Figure 2.22 Representation of two-port scattering parameters system

Mathematical representation of the two-ports s-parameters network is shown in equation 2.50. Here, S_{11} is named as a return loss or reflection coefficient. a_1 and a_2 feed the system through port 1 or 2 or express the incident waves in the case of wave transmission. b_1 and b_2 express the reflected waves in the case of wave transmission.

$$\begin{bmatrix} b_1 \\ b_2 \end{bmatrix} = \begin{bmatrix} S_{11} & S_{12} \\ S_{21} & S_{22} \end{bmatrix} \begin{bmatrix} a_1 \\ a_2 \end{bmatrix} \quad (2.50)$$

In case of power supply from port 1, $a_2 = 0$ and S_{11} is calculated as

$$S_{11} = b_1/a_1 \quad (2.51)$$

S_{21} expresses forward transmission coefficient which can be calculated with condition $a_2 = 0$ as

$$S_{21} = b_2/a_1 \quad (2.52)$$

The calculation of backward transmission coefficient (S_{12}) can be determined by $a_1 = 0$ as

$$S_{12} = b_1/a_{12} \quad (2.53)$$

S_{22} is called the return loss or reflection coefficient for the port 2 and is calculated as

$$S_{22} = b_2/a_2 \text{ , } a_1 = 0 \quad (2.54)$$

Determination of how much power a solar cell gains depends on ability of solar cell absorption from incoming electromagnetic radiations. According to general formula of the absorption (A=1-R-T) shown in equation (2.55), high transmission and reflection coefficient decrease the power gained by the solar cells.

$$A\,(\omega) = 1 - |S_{11}(\omega)|^2 - |S_{12}(\omega)|^2 \quad (2.55)$$

$$S_{11}(\omega) = \frac{\sqrt{power\ reflected\ from\ port\ 1}}{\sqrt{power\ incident\ on\ port\ 1}} \quad (2.56)$$

$$S_{12}(\omega) = \frac{\sqrt{power\ delivered\ to\ port\ 2}}{\sqrt{power\ incident\ on\ port\ 1}} \quad (2.57)$$

$S_{11}(\omega)$ and $S_{12}(\omega)$ are the scattering parameters which are functions of power flow from reflected and transmitted radiations respectively. $A\,(\omega)$ is power gain by solar cell. Our aim is optimize the power gain which is possible with minimize reflected and transmitted radiations. In this context, transmission losses are reflected by employing metalic ground plate for the proposed solar cell absorber. The equation of the the absorption (A=1-R-T) replaced by the terms that shown in equation (2.58)

$$A\,(\omega) = 1 - |S_{11}(\omega)|^2 \qquad (2.58)$$

CHAPTER 3

RESULTS AND DISCUSSION

3.1 Electromagnetic Spectrum

The electromagnetic spectrum is the concept that expresses all the electromagnetic radiation made possible by the laws of physics in the universe and the relative locations of these spectra according to the wavelengths or frequencies of different radiation derivatives. The radiation types in the electromagnetic spectrum, starting from high energy to the low energy region.

Our study is about investigation of MXene as a dielectric layer of solar cell absorber in 420 -1000 nm that cover visible frequency range. Visible light covers the rays between 400 and 700 nanometers wavelength. This small part of the electromagnetic spectrum, called light, can be seen by humans. The visible light spectrum has some colors depends on frequency or wavelength as shown in Figure 3.1. From high energy (frequency) to low energy (frequency) it can be listed as purple, blue, green, yellow and red.

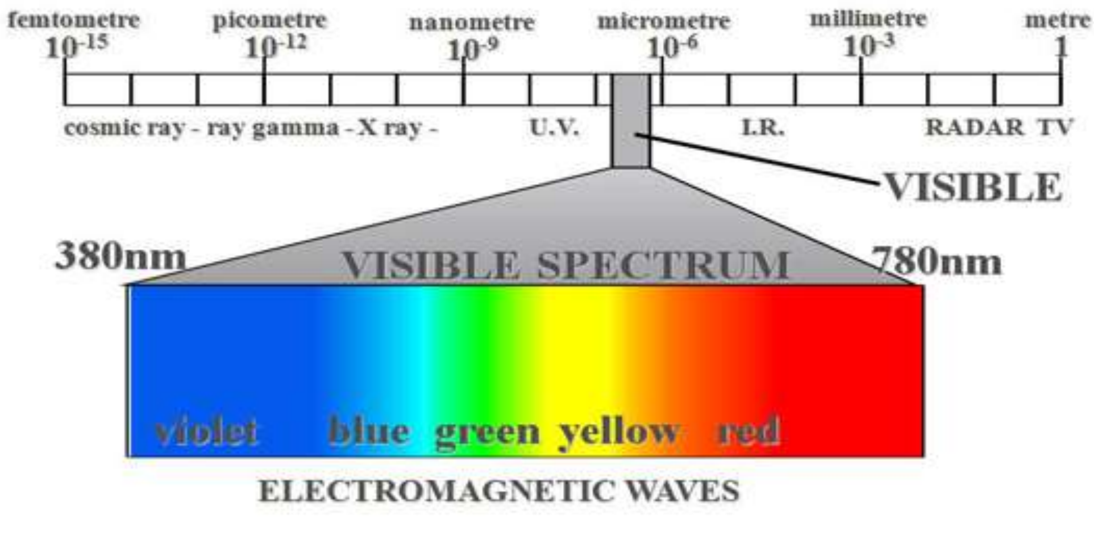

Figure 3. 1 Representation of electromagnetic spectrum.

Although the wavelengths and so the frequencies of the electromagnetic waves are different, the propagation velocities are the same. This velocity is equal to the speed of light in the space and is approximately shown in equation (3.1)

$$c = 300000 \text{ km/h} \tag{3.1}$$

The relation between frequency and wavelength is

$$c = \lambda .f \tag{3.2}$$

It is known that distance is the product of velocity and time. When this formula is applied to the electromagnetic wave, it can be replaced by λ (wavelength) instead of distance, T (period time) instead of time, c light speed instead of velocity. There is an inverse proportionality between wavelength and frequency. This means that the wavelength of the high-frequency is short and the wavelength of the low frequency is long [47].

3.2 CST Microwave Studio

Computer simulation technology microwave studio is a software that can provide electromagnetic design and analysis in the high frequency range by a powerful graphical solid modeling. An important feature of CST microwave studio is options that choice of simulator or mesh type for a particular problem, integration into one user interface smoothly.

The CST microwave studio software include various different simulation techniques such as time domain solvers, frequency domain solvers, asymptotic solver, integral equation solver, multilayer solver and eigenmode solver for specific suit various applications. The frequency domain solvers are more efficient than time domain solvers for structures that are much smaller than the shortest wavelenght of interest. Also the frequency domain solver is method of choise for narrow band problems such as filters. Frequency domain solvers generate broadband results by using fast reduced order model techniques. The frequency domain solver support tetrahedral and hexahedral meshes. One of the other important feature of software is full parameterization of the structure modeler that offers using of variables in the description of all geometrical and material properties of component. As a result, CST microwave studio is built-in optimizer and parameter sweep tools and capable of the design and analysis of electromagnetic devices.

3.3 Thin Film (6,5) Semiconducting Single Walled Carbon Nanotube Metamaterial Absorber for Photovoltaic Applications

As we mentioned before there are some publications about using of two dimensional material for solar cell applications. In this section we explained the article of thin film (6,5) semiconductıng single-walled carbon nanotube metamaterial absorber for photovoltaic applications is one of the example for this publications that we taked reference during process of this study. Obaidullah et all. design and analyzed solar cell absorber in visible and ultraviolet frequency region. Single-walled carbon nanotube with chiral (6,5) used as a two dimensional material [9].

3.3.1 Introduction

Electromagnetic response of (6,5) semiconducting single-walled carbon nanotube as an dielectric material between top aluminum resonator and bottom aluminum ground plate numerically simulated and analyzed in this publication. In order to check absorption values for geometric parameters of structure changed and observed that reflection of proposed design changes with changing geometric parameters.

3.3.2 Material properties extraction

First step for the designing carbon nanotube absorber is to determine the frequency dependent material properties such as permeability and permittivity for single wall carbon nanotube in the frequency range of interest. Experimental or measured scattering parametres (s-parameters) are required for determine permeability and permittivity. Nicolson Rose Weir (NRW) technique is used for determine the effective permittivity and permeability of single walled carbon nanotube with different chiralities. The s-parameters plots of the given permeability and permittivity for carbon nanotube film in Reference 48 are digitized and used in NRW algorithm to find dielectric constant of carbon nanotube as shown in Figure 3.2.

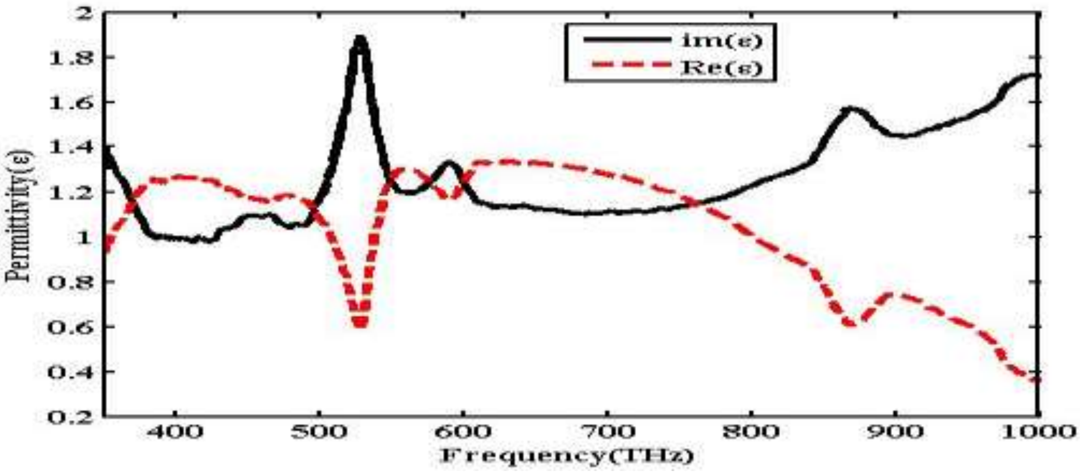

Figure 3. 2 Real and imaginary part of the permittivity for (6,5) chirality.

3.3.3 Design and Analysis

The proposed single walled carbon nanotube metamaterial absorber consist of three layers. These are aluminum metalic bottom ground plate with thickness ‘‘h’’, (6,5) single walled carbon nanotube as a dielectric layer on the top of ground plate with thickness ‘‘d’’ and aluminum resonator at the top of dielectric layer with thickness ‘‘t’’ as shown in Figure 3.3. The dielectric constant of aluminum is taken from study of palik. Optimal dimensional values of proposed design are achieved by changing and simulating all parameters together shown in Table 3.1.

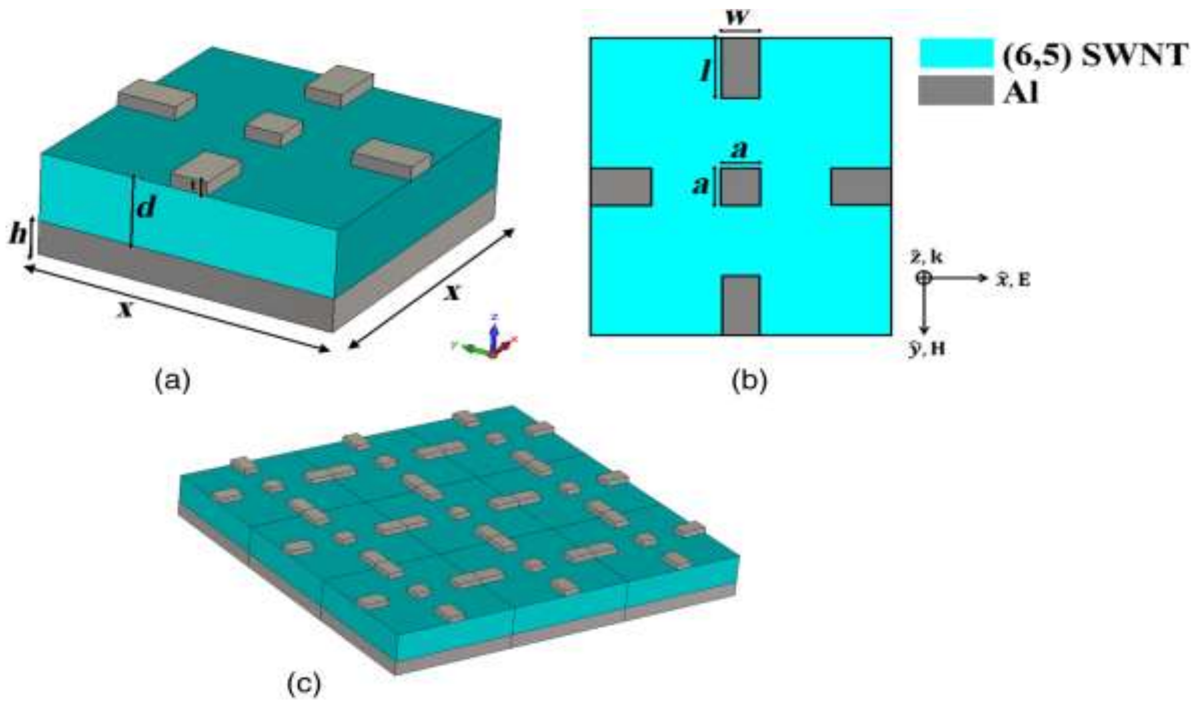

Figure 3.3 (a) View of proposed design and geometric parameters of (6,5) SWNT metamaterial absorber, (b) top view of the design, and (c) complete proposed absorber design [48].

Parameter	Value (nm)
a	50
d	100
h	50
l	80
t	20
w	50
x	400

Table 3. 1 Dimensional values of proposed absorber design.

Generation of the wide band absorption in frequency of interest depend on geometric configuration of resonator which consist of a central patch and four identical strips. Full wave electromagnetic solver used for computationally analysis of proposed design and solve maxwell equation. All simulations are executed with a transverse electromagnetic (TEM) waves and proposed design operates in 350 to 1000 THz frequency region.

3.3.4 Results and Discussion

Absorption and reflection plots of proposed design that obtained after simulation in visible and ultraviolet frequency region are shown in Figure 3.4. The combination of resonant frequencies generate a wide band absorption. High absorption occur with result of spectral matching of single walled carbon nanotube with the metamaterial resonance. Four different frequencies was emphasised such as 450 THz, 500 THz, 627 THz and 750 THz which absorption rate are 97.4 %, 98.3 %, 99.2 % and 98.4 %, respectively.

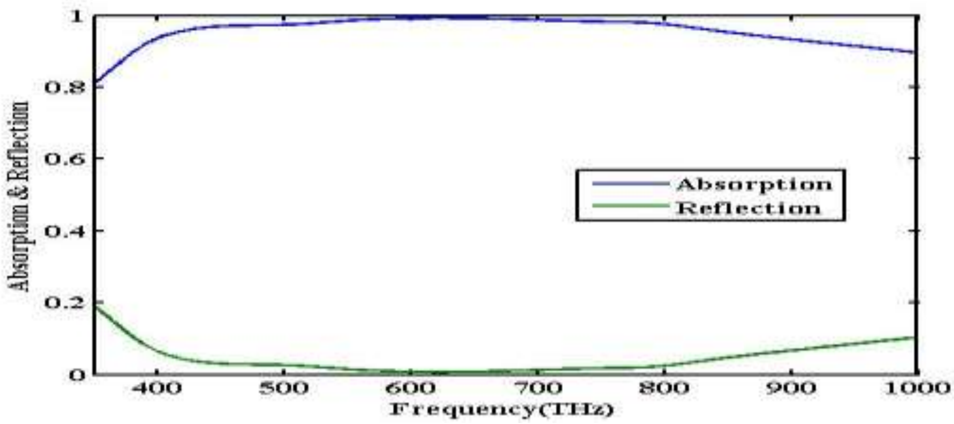

Figure 3.4 Absorption and reflection plots of proposed design in the visible and ultraviolet frequency region.

Strong coupling of each strip resonator and central patch with the ground plate and the dielectric layer generate wide band absorption. In order to understand mechanism of the wide band absorption, numerical simulation for a single, double, triple and quadruple strips with center patch were done. The absorption plots of single, double, triple and quadruple with the center patch shown in Figure 3.5, respectively. From the Figure 3.5 it can be clearly observed that absorption rate is increase when number of strips increase double and triple. Also maximum absorption (99.2 %) at 627 THz is achieved in case of quadraple strips.

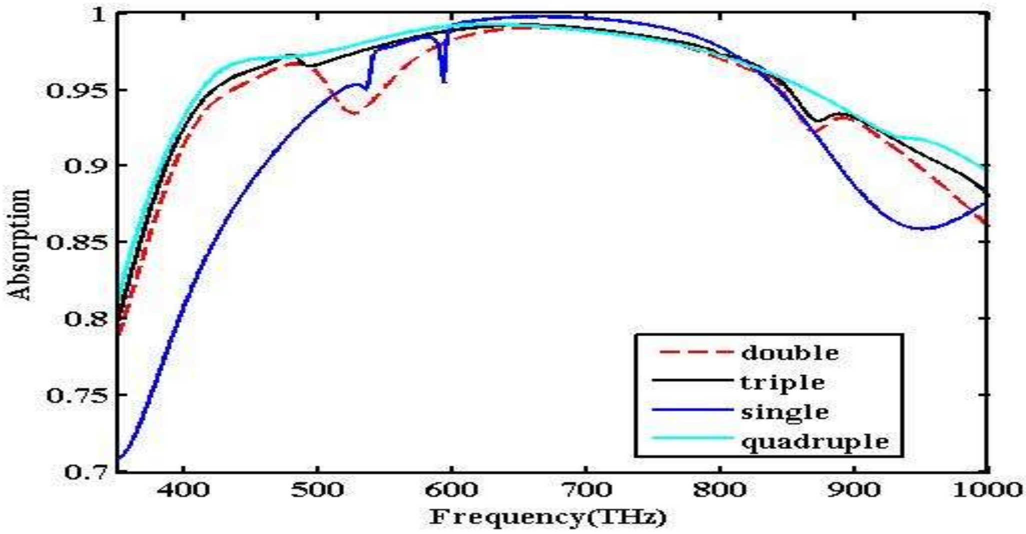

Figure 3.5 Absorption behavior of the single, double, triple and quadruple strips with the center patch.

3.3.5 Polarization and Incident Angle

In order to further analysis the absorption behavior of proposed design related to radiation sources, simulations under different incidence angles for transverse electric (TE), transverse magnetic (TM) modes and for different polarization angles (TEM mode) are executed. Simulation results of absorption spectra for TE mode given in Figure 3.6 and Figure 3.7 shows difference in absorption spectra for TM mode. From the Figure 3.6 and 3.7 it can be observed that the incident angles for TE mode highly sensitive than TM mode, especially for 60 degree and 75 degree whichs have minimum absorption rates. Incident wave which dependent of strength of magnetic field component has angle of incidence θ which becomes smaller in case of θ increases. Thus, at larger incident angles such as 60 degree and 75 degree, the magnetic polaritons are not efficiently excited which increase reflection of incident waves and decrease amount of absorption by impedance mismatch.

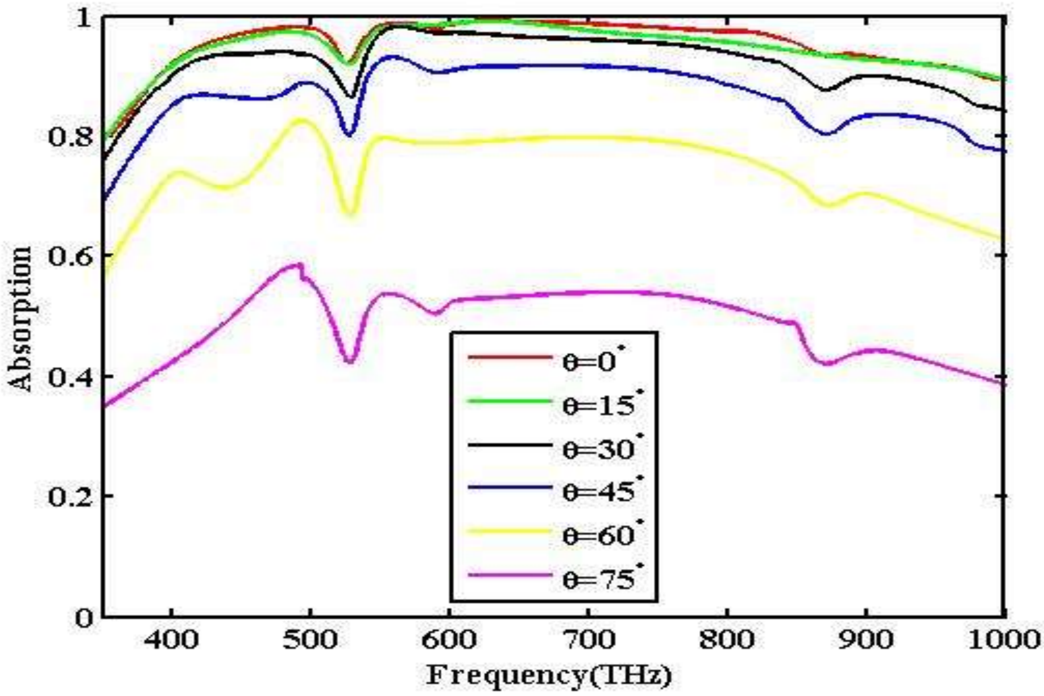

Figure 3. 6 Absorption spectra of different incident angles for TE mode.

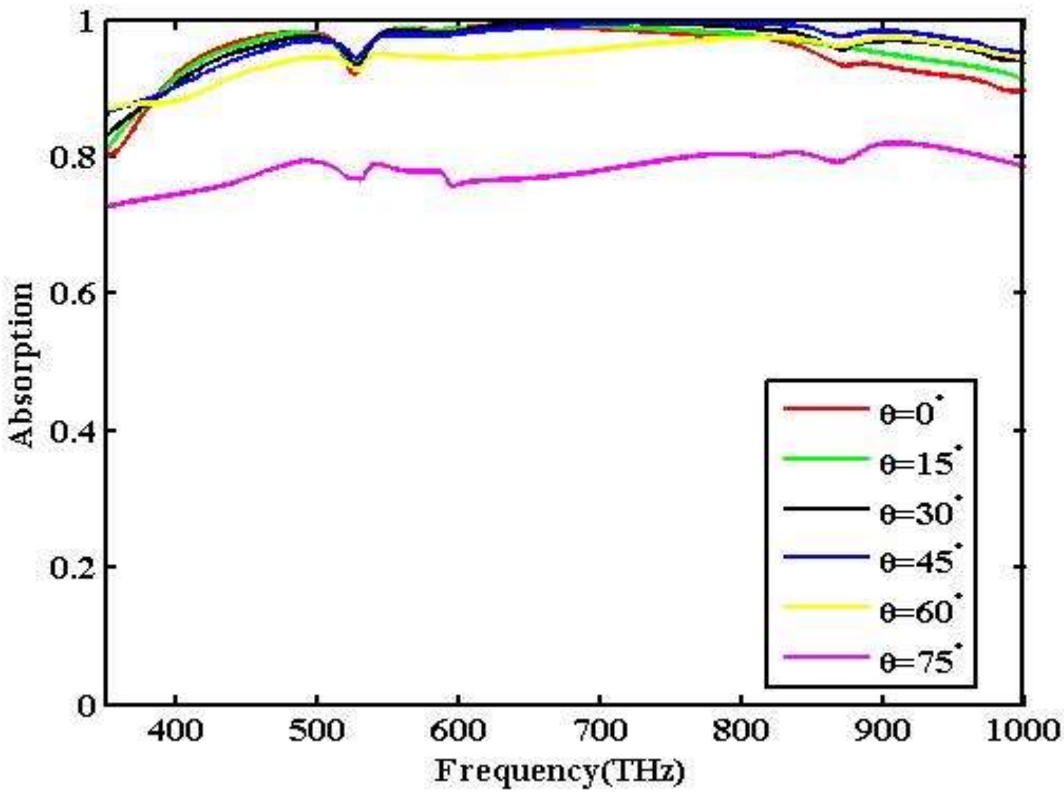

Figure 3. 7 Absorption spectra of different incident angles for TM mode.

Symmetric characteristics of proposed design provides independency of polarization angles from 0 degree to 90 degree under normal incidence (TEM mode) illustrated in Figure 3.8.

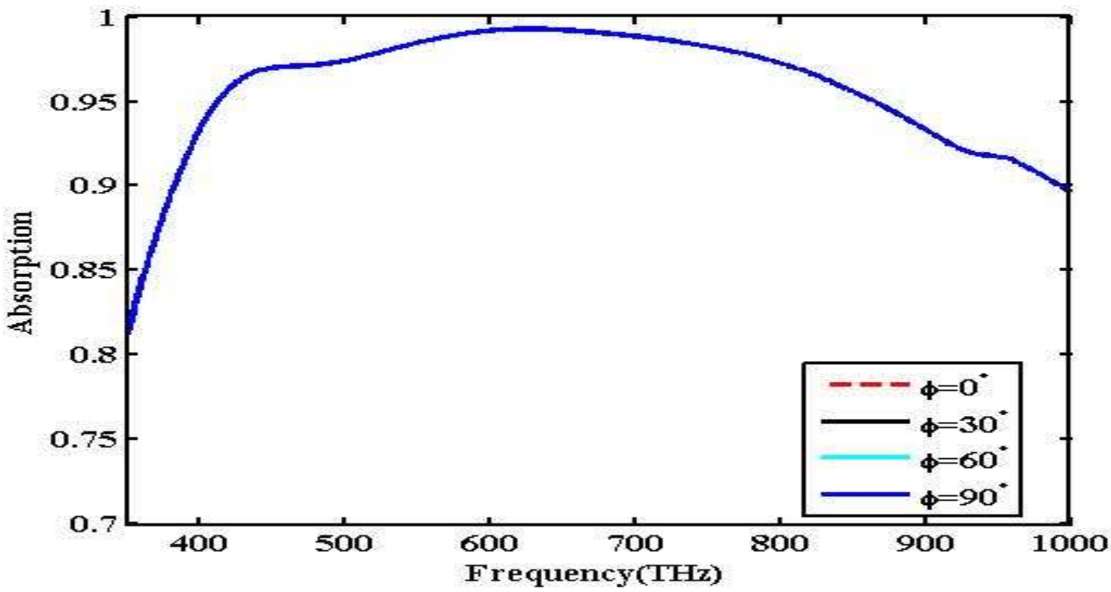

Figure 3.8 Absorption spectra of different polarization angles for TEM mode.

3.3.6 Conclusion

(6,5) single walled carbon nanotube metamaterial absorber investigated in the visible and ultraviolet frequency. The proposed design achieved 99.2 % absorption rate as a result of strong electric and magnetic fields between the ground metalic plate and the resonator strips. Absorption simulations are executed under different polarization and incident angles to show proposed design is independent from polarization angles.

3.4 The Proposed MXene Based Metamaterial Absorber for Solar Cell Applications

3.4.1 Introduction

In the previous sections, we explained that (6,5) semiconducting single walled carbon nanotube used as active layer for solar cell absorber in the visible and ultraviolet frequency region. Here, for the first time, MXene ($Ti_3C_2T_x$) based metamaterial absorber for solar cell applications designed and simulated in visible frequency region via CST microwave studio software. Basically, we used MXene

($Ti_3C_2T_x$) as active layer in this study instead of (6,5) semiconducting single walled carbon nanotube to demostrated that MXene as a novel member of 2D material family has high absorption potantial for solar cell applications. The thickness of the materials that we used in our structure are less than (6,5) single walled carbon nanotube. In this section we explained some steps such as material properties extraction of MXene, design and simulation of proposed structure with its geometrical parameters, simulation result of absorption and reflection, absorption spectra of different incident for TE and TM mode, absorption spectra of different polarization angles for TEM mode, fields and current distributions of proposed design.

3.4.2 MXene based metamaterial absorber for solar cell applications

3.4.2.1 Structure Design and Simulation

In this section, a MXene based metamaterial absorber is designed. First of all due to MXene is a new material, CST microwave studio is not include dielectric constant of MXene material in its material library. Thus, we have to obtain MXene dielectric constants for adding simulation program. After long literature research, we found a publication about experimentally measured real and imaginary permittivity of MXene ($Ti_3C_2T_x$) film that measured with a variable angle spectroscopic ellipsometry (VASE) set up. On the purpose of extract the parameters of dielectric constant and fit the measured raw VASE, two lorentz oscillators and one drude term are used. Two Lorentz oscillators used for the inter-band electron transition and the drude term represent the metal-like behavior. The result of measured, plots of real and imaginary parts of permittivity for ($Ti_3C_2T_x$) film versus wavelenght (nm) are obtained [49]. We digitized plots of real and imaginary parts of permittivity for ($Ti_3C_2T_x$) film and converted wavelenght (nm) to frequency (THz) for adding material library of CST microwave studio software.

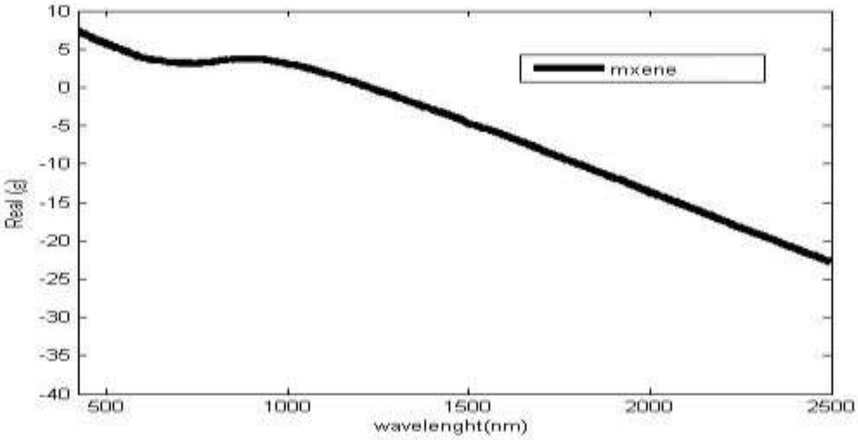

Figure 3.9 Digitized plots of real part of permittivity for $Ti_3C_2T_x$ film.

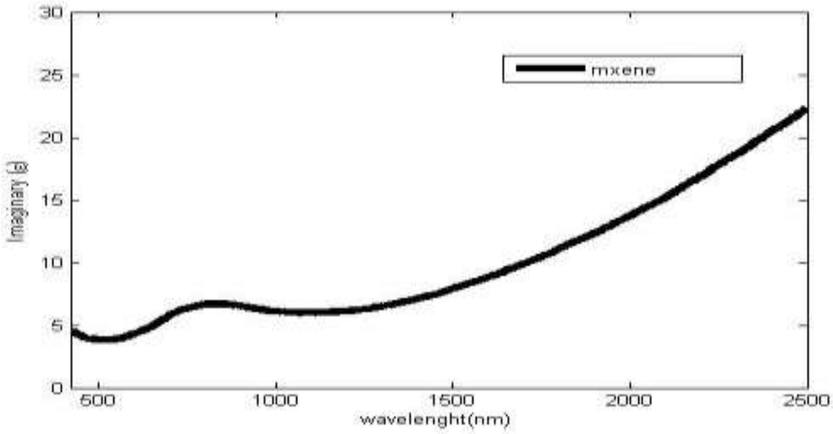

Figure 3.10 Digitized plots of imaginary part of permittivity for $Ti_3C_2T_x$ film.

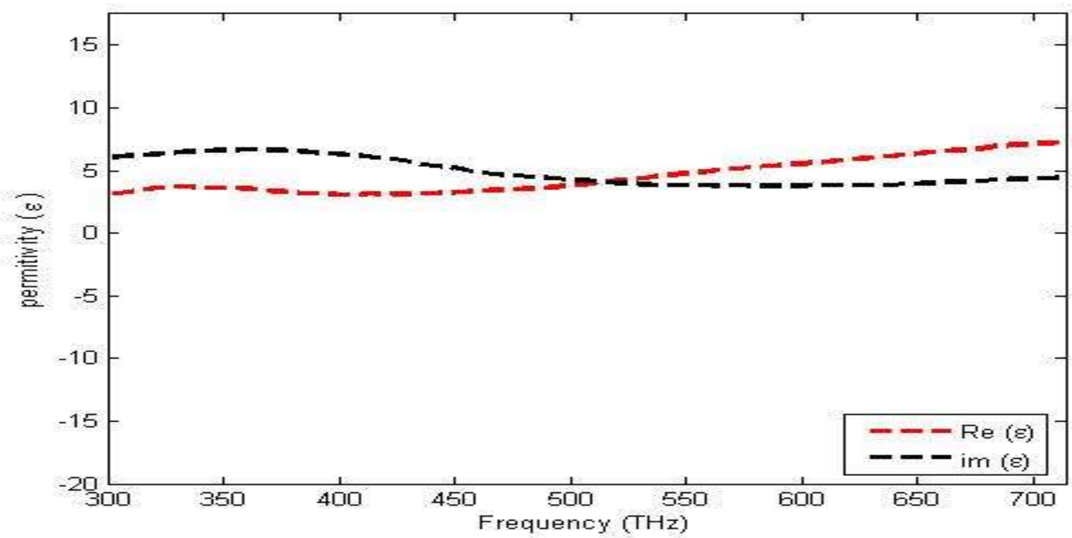

Figure 3. 11 Exracted real and imaginary part of the permittivity for $Ti_3C_2T_x$.

The proposed MXene based metamaterial absorber unit cell consist of three basic parts: aluminum resonator at the top of the structure, aluminum metalic bottom ground plate and MXene as a dielectric layer in between metalic top resonator and bottom ground plate as shown in Figure 3.12.

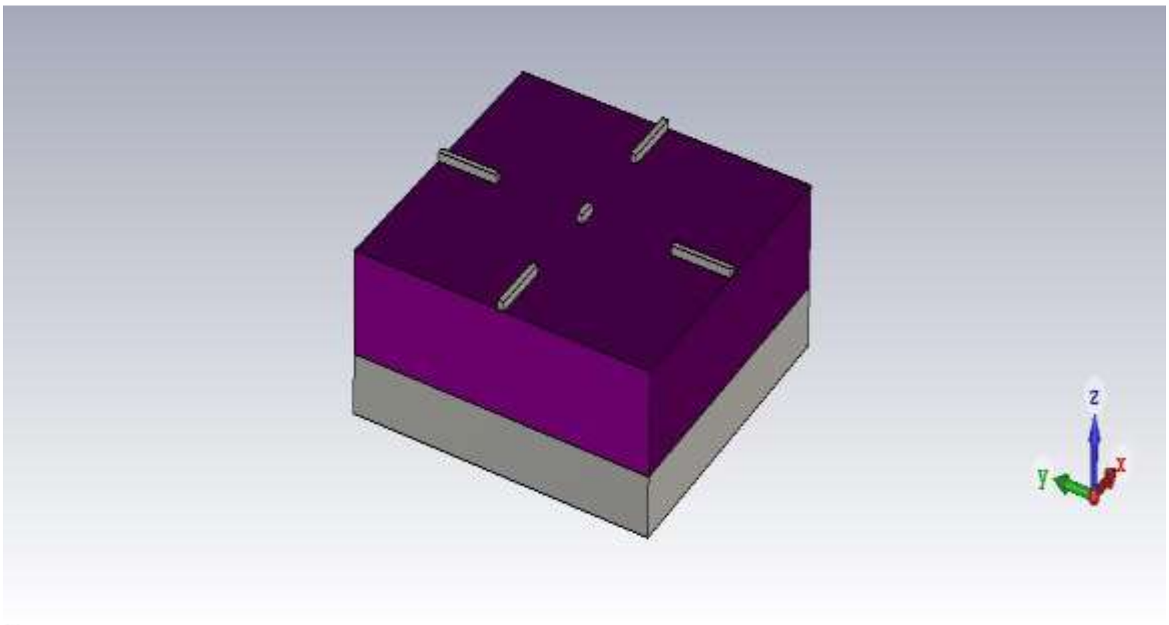

Figure 3. 12 Perspective view of unit cell.

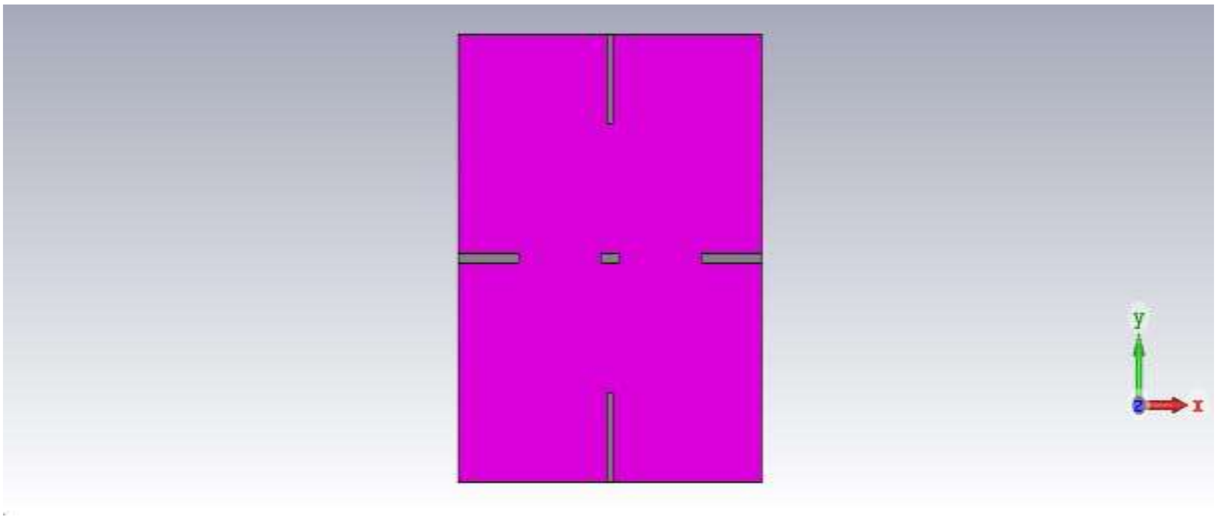

Figure 3.13 Top view of the design.

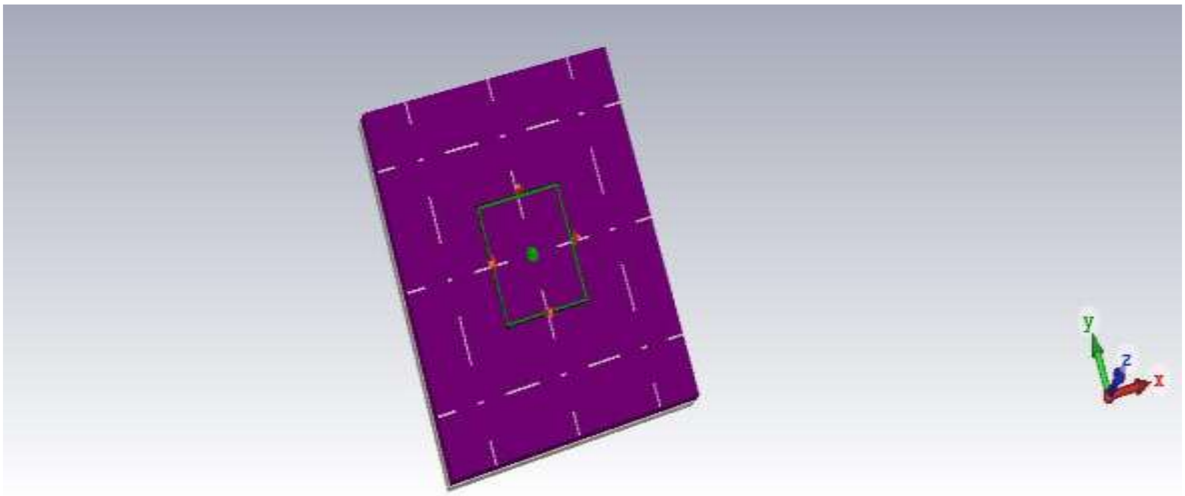

Figure 3. 14 Complete proposed absorber design.

The MXene layer with thickness ‘’m’’ is coupled with aluminum bottom ground plate with thickness ‘’a’’ and the aluminum metalic top resonators with thickness ‘’r’’ in order to enhance the resonance frequencies. Aluminum is selected for low skin depth, low cost, resistance to high temprature, have ability to reflect in high frequency radiations [50]. The dimensional characteristic of the proposed design is given in Table 3.2. The maximum absorption achieved with arrangement, orientation and geometric configuration of resonators in the proposed design. The resonator geometric configuration consist of the four identical strips and a central patch which is in the middle of the four strips. The lateral dimension of the structure (a + m + r) must be less than the wave lenght of the incident radiations [51].

Parameter	Value (nm)	Explanation
a	32	Thickness of aluminum ground plate
b	8	Width of resonators
d	80	Length of strips
e	25	Length of central patch
k	400	Peridiocity of structure
m	55	Thickness of MXene layer
r	5	Thickness of resonators

Table 3. 2 Geometrical dimensions of the proposed absorber design.

The simulation for the oriented MXene based metamaterial absorber is operated with full wave electromagnetic software established on Finite Integration Technique (FIT), with frequency domain solver. The proposed design operated at frequency ranging from 300 THz to 714 THz. The direction of incident electromagnetic radiations is E-field along x-direction and H-field along y-direction and both E-field and H-field propagate paralel to the structure plan. In addition, wave vector (k) is perpendicular to the absorber [52], the boundary conditions selected periodic in both x- and y- plane and open add space in the z-plane. Mesh type of simulation was is selected tetrahedral mesh, the minimum and maximum number of passes per wavelength selected 4 and 10, respectively.

3.4.2.2 Results and Discussion

The optical absorption depends on its reflection and transmission coefficient that can be formulated as A=1-R-T. The bottom aluminum metalic plate behave like a mirror and block transmission [53]. We observed that transmission plots of design is almost zero, so we assumed that A=1-R for our design to calculate absorption. We taked free-space impedance as 377 Ω is match with impedance of proposed design. This calculation and simulation process results in achieving the minimum reflection rate which leads to higher absorption in the frequency range of interest.

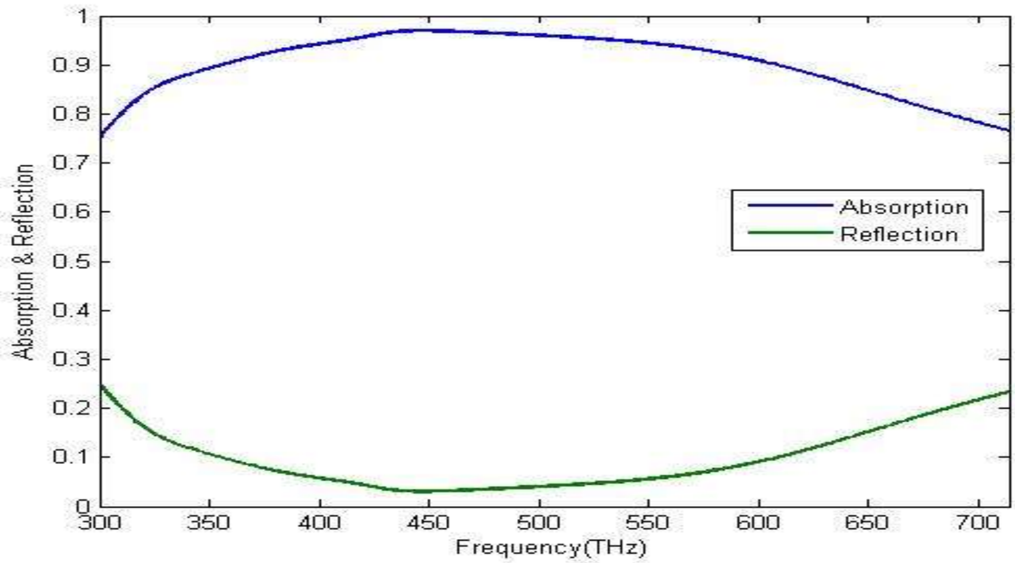

Figure 3. 15 Absorption and reflection curves of the proposed absorber design in 300 THz to 714 THz frequency region.

Strong coupling of each strip resonator and central patch with MXene and aluminum layer is provided electromagnetic response of wide band absorption. Simulation result for absorption and reflection of the unit cell absorber design in frequency ranging from 300 THz to 714 THz shown in Figure 3.15. Absorption rate is more than 90 % in between 360 THz to 603 THz frequency region. Proposed design that we simulated achieved 96.8 % maximum absorption at 450 THz.

3.4.2.2.1 Geometric parameters study

Geometric arrangement of structure effect the absorption rate of design inevitably. For this reason parametric analysis is done to show the effect of the geometry on the absorption behaviour. Consider that best chosen results are shown with black color in all plots in this section. First, dielectric thickness ‘‘m’’ investigated by keeping other parameters constant. The thickness of dielectric increased and decreased from 55 nm with 10 nm steps as shown in Figure 3.16 (a). The absorber design is sensitive to increasing or decreasing of dielectric thickness especially for frequency between 300 THz to 500 THz range for m<55 nm and m>55 nm. The maximum absorption achieved with thickness m=400 nm.

The maximum absorption achieved by the impedance matching at resonance frequency in case of magnetic resonance generate by electric resonance from the between the top aluminum resonator and bottom metalic layer.

The behavior of increasing and decreasing the thickness of resonator by 1 nm steps as shown in Figure 3.16 (b) shows that proposed design have high absorption at r=5 nm than the other thickness around 450 THz frequency.

The length of strips ''d'' is an important parameter for configuration of resonators which effects absorption ratio with small difference at around 450 THz as shown in Figure 3.17 (b). The maximum absorption achieved with thickness d=80 nm. The peridiocity of the proposed design with thickness ''k'' investigated by increased and decreased by 10 nm steps to show behavior of absorption as shown in Figure 3.17 (a). Proposed design have low absorption at 300 THz to 500 THz when k<400 nm and k>400 nm thickness. The maximum absorption achieved with thickness k=400 nm.

The absorption behavior for width of resonators with length ''b'' and length of central patch ''e'' are shown in Figure 3.18 (a) and (b), respectively. Nearly same absortion behaviour was observed at frequency range of interest. The length of ''b'' increased and decreased by 1 nm steps and observed that best absorption achieved with b=8 nm. The length of central patch achieved peak absorption with e=25 nm in result of increased and decreased the length by 5 nm steps.

a)

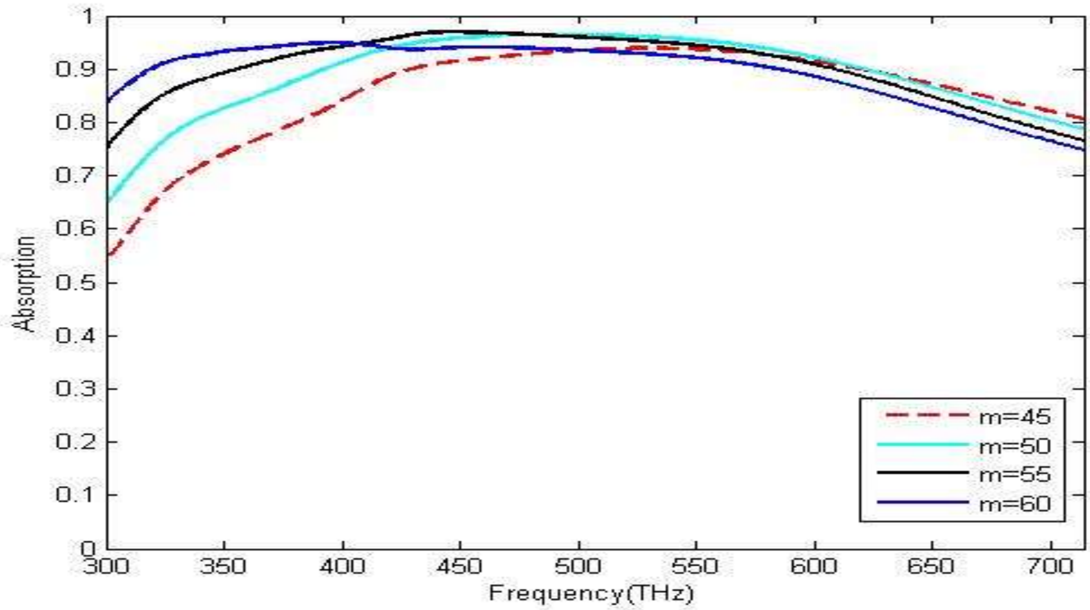

b)

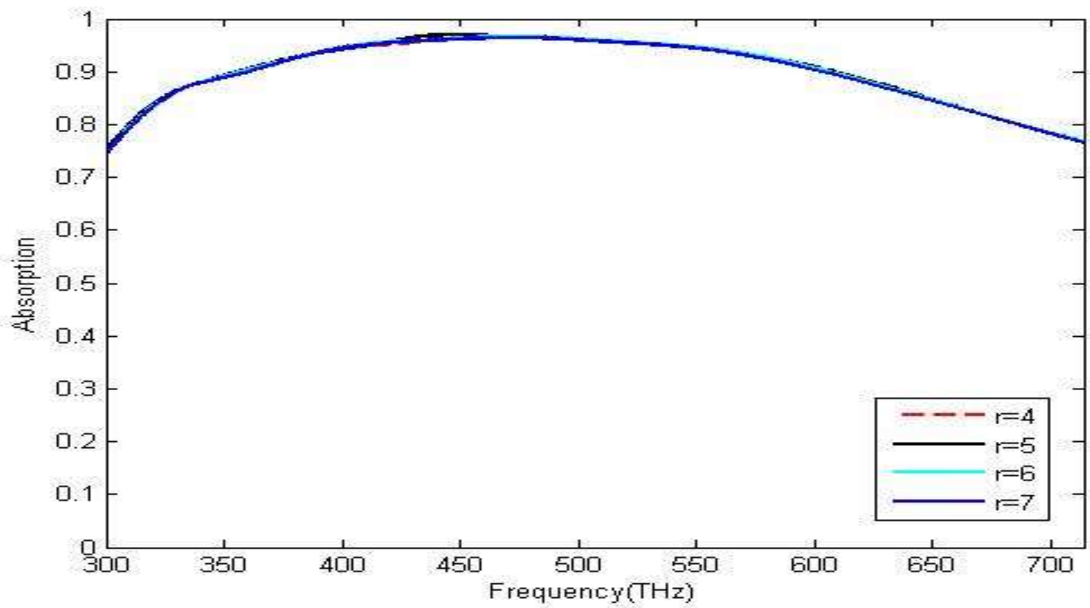

Figure 3. 16 Simulated absorption result for (a) thickness of MXene ‘‘m,’’ (b) thickness of the resonators ‘‘r. ’’

a)

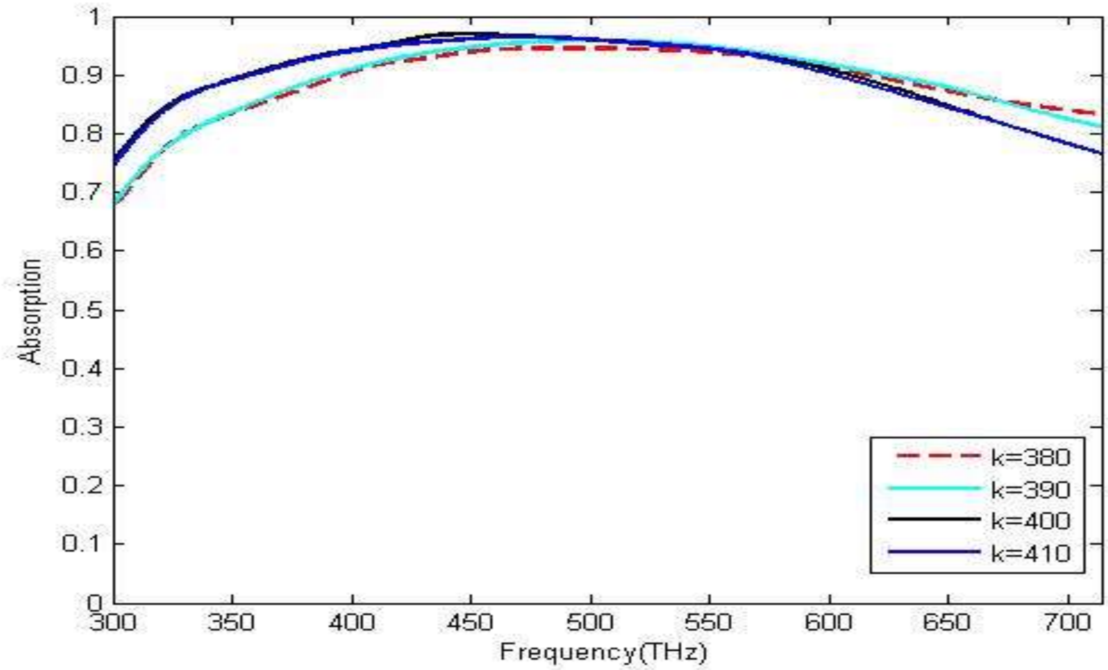

b)

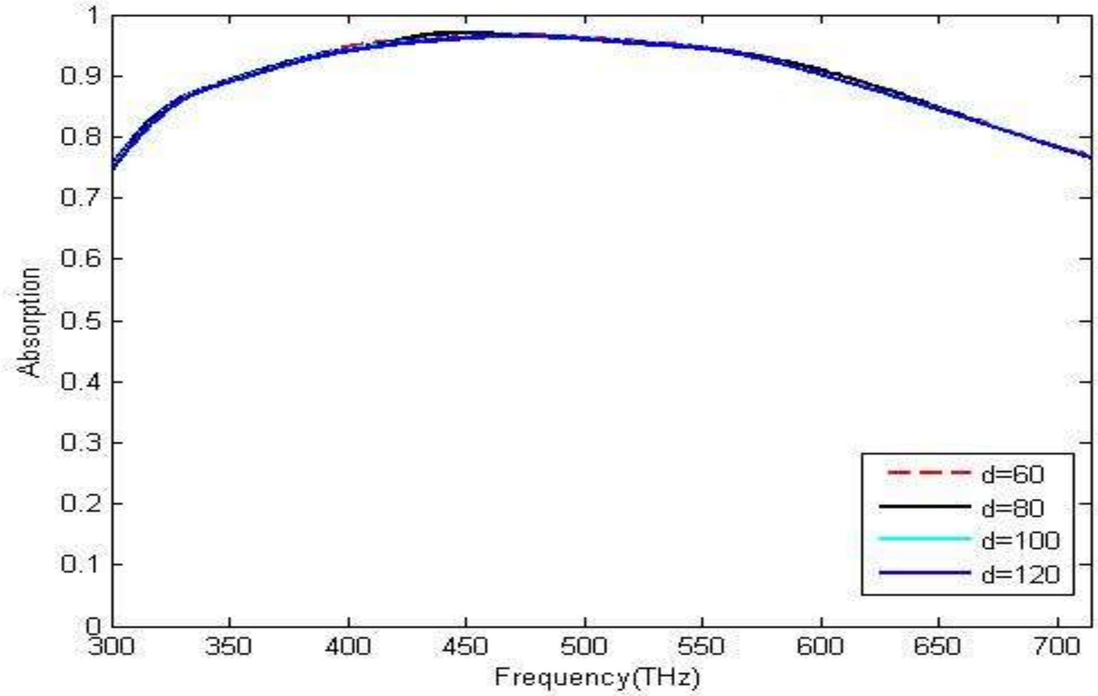

Figure 3. 17 Simulated absorption result for (a) absorber peridiodicity ‘‘k,’’ (b) length of strips ‘‘d. ’’

a)

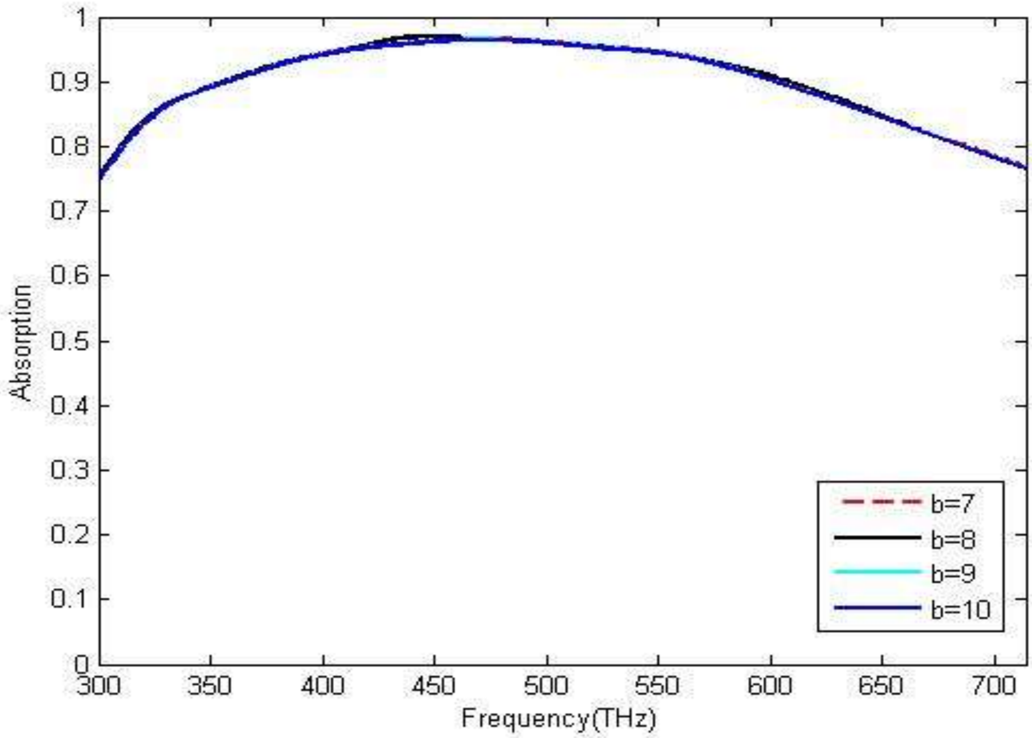

b)

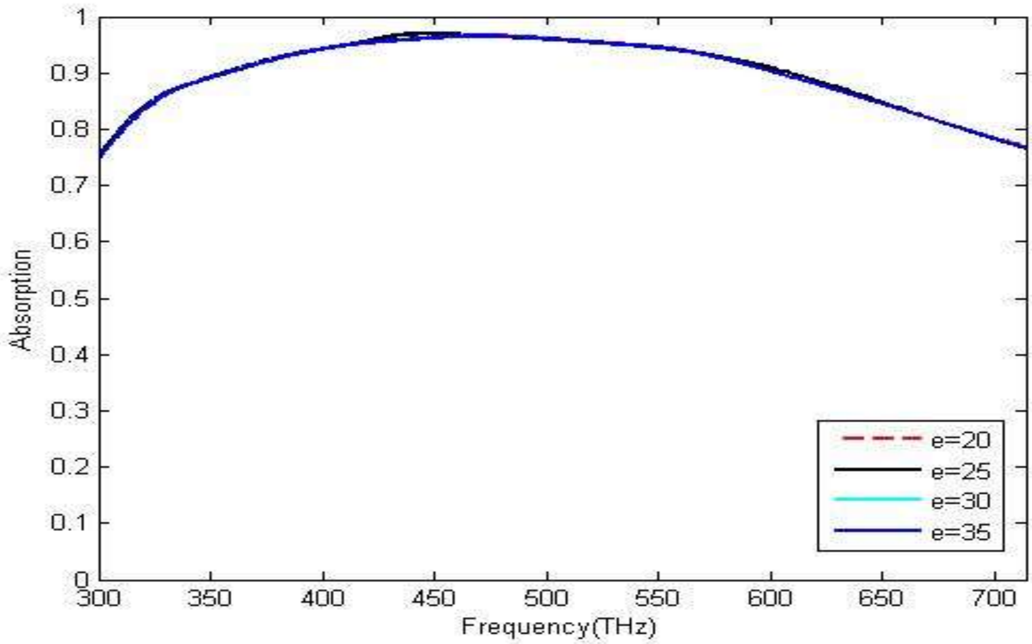

Figure 3. 18 Simulated absorption result for (a) width of the resonators ‘‘b,’’ (b) length of the central patch ‘‘e. ’’

3.4.2.2.2 Fields and Surface Current Distributions Analysis

In order to realize the physics behind absorption mechanism of proposed MXene based metamaterial design, electric and magnetic field distribution and surface current distribution at four resonant frequencies 380 THz, 450 THz, 525 THz, 600 THz are investigated and illustrated in Figure 3.19, Figure 3.20 and Figure 3.21 respectively. It can be seen from the results, the strong electric field is localized around center patch and resonator strips show importance of coupling of resonators.

The electric field distribution almost proportional with the absorption at specified resonant frequency. The intension of electric fields localized around the resonators promote charge on the surface of structure that lead to generate circulating current. The circulating current induce with the coupling between resonator strips and bottom plate. Magnetic field distribution at 380 THz localized between two horizantal strips and bottom layers. Also the strong magnetic field distribution can be seen in surface of structure at 600THz. Although surface current represent that parallel current is moving through the MXene layer, a minimum amount of circulating current is seen at the resonator strips.

The result of simulation for electric and magnetic field and current distribution refer that impedance of proposed design accord with free space impedance. This matching lead to maximum absorption of electromagnetic waves at wide band frequency region.

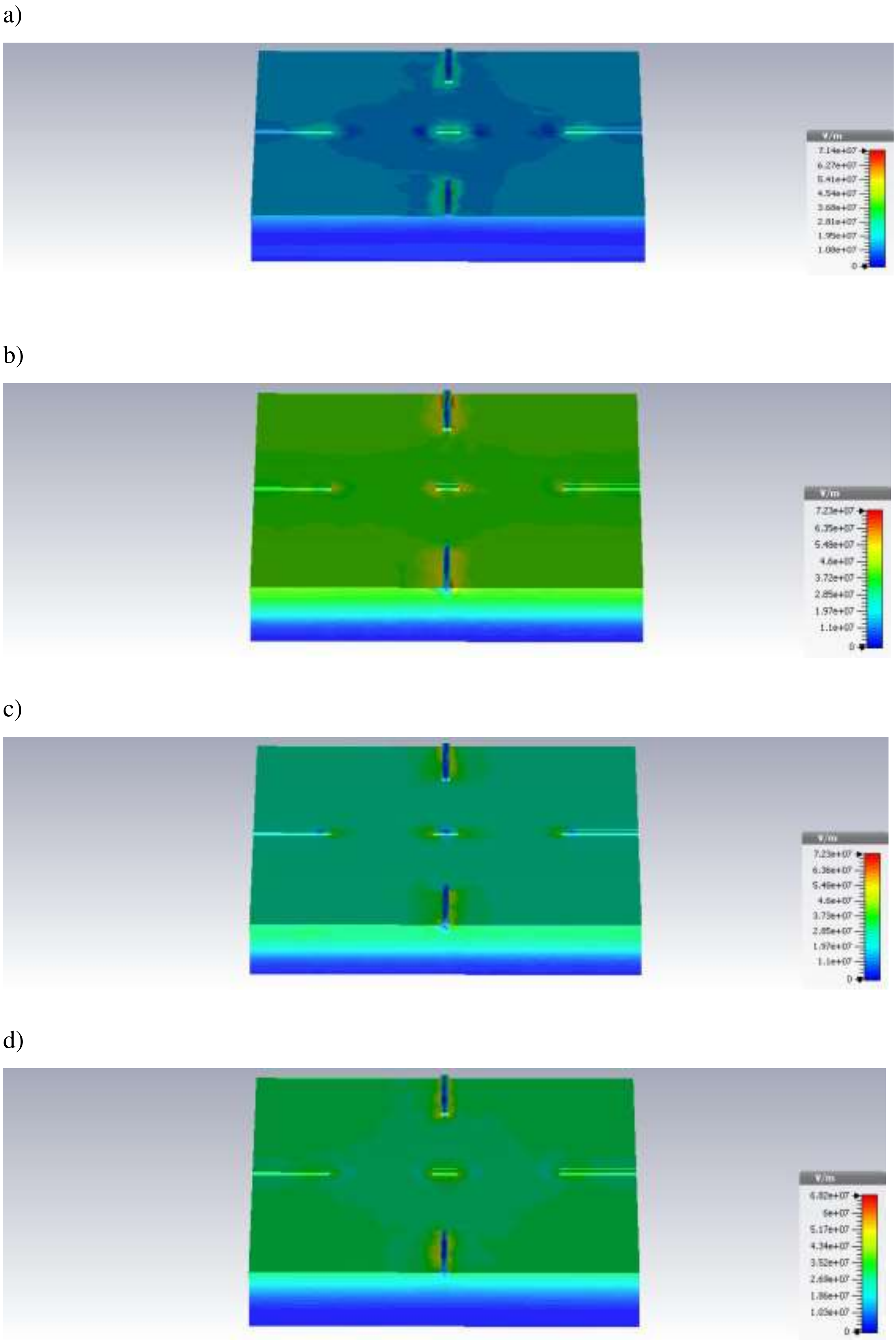

Figure 3. 19 Electric field distribution of the absorber design at (a) 380 THz, (b) 450 THz, (c) 525 THz and (d) 600 THz.

a)

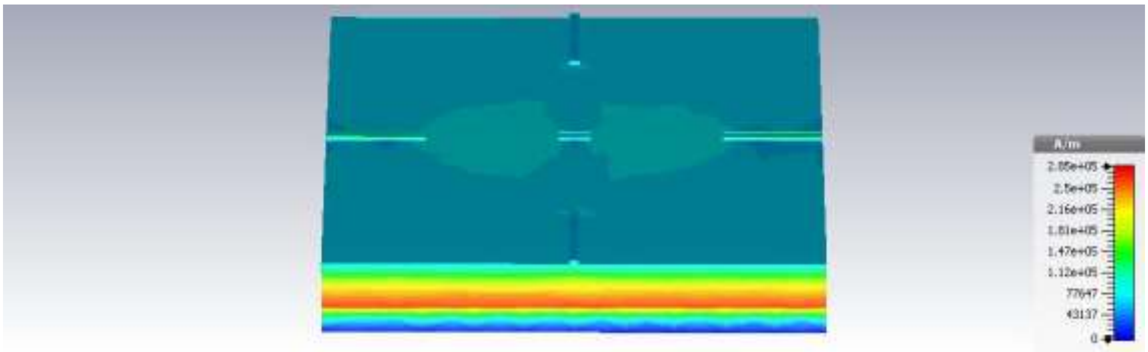

b)

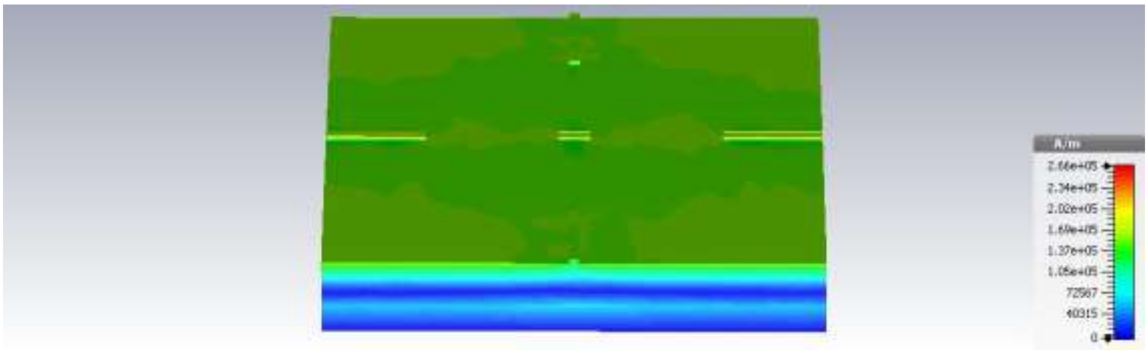

c)

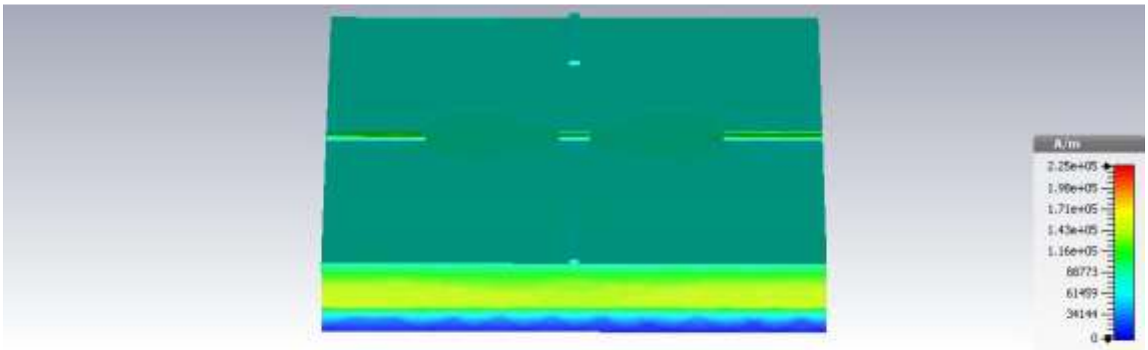

d)

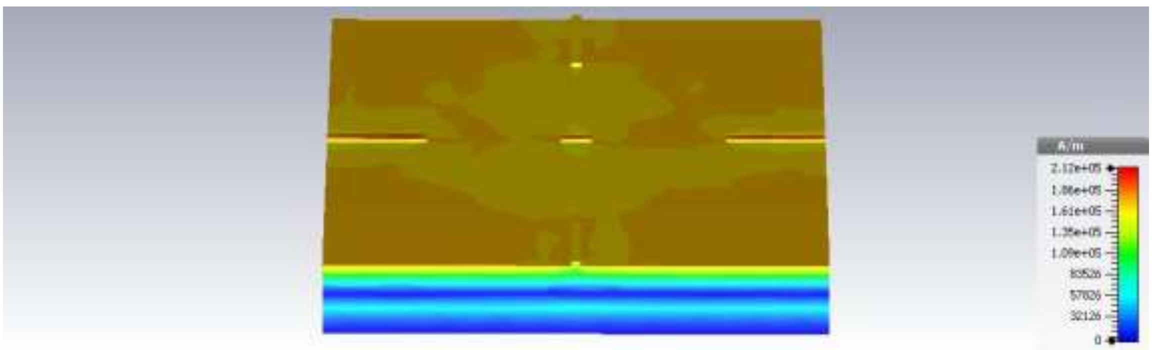

Figure 3.20 Magnetic field distribution of the absorber design at (a) 380 THz, (b) 450 THz, (c) 525 THz and (d) 600 THz

a)

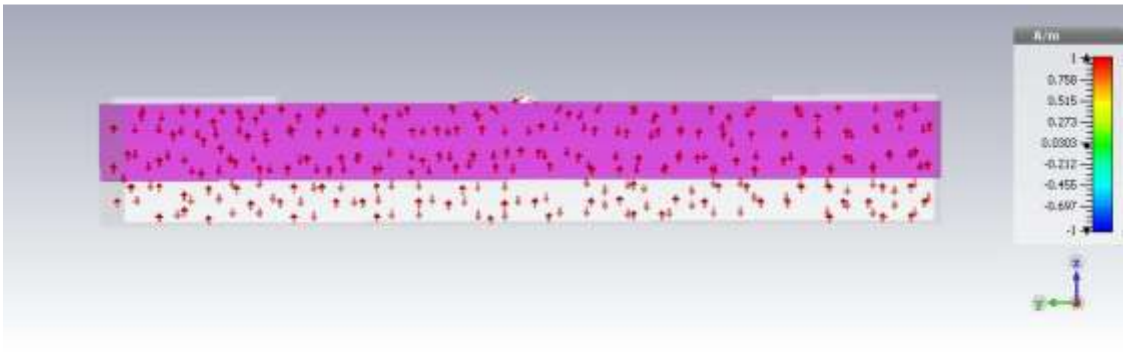

b)

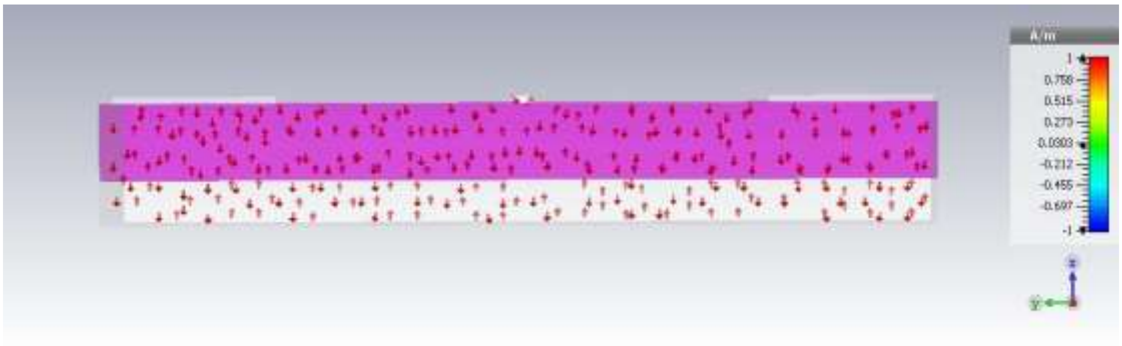

c)

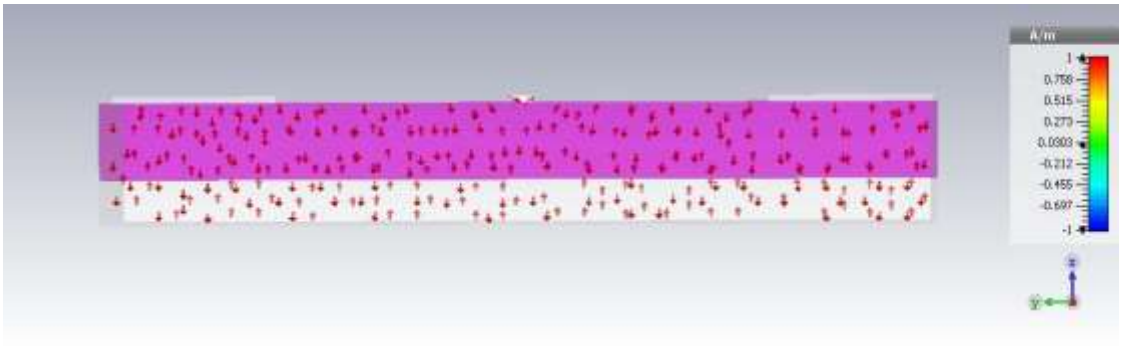

d)

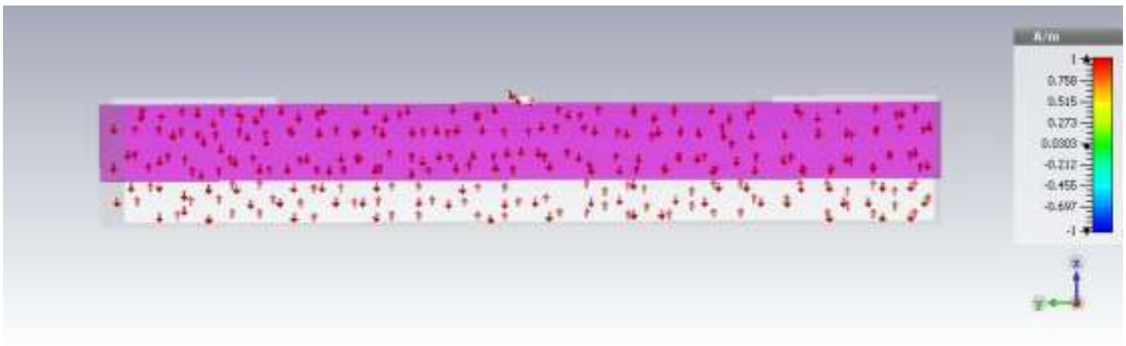

Figure 3.21 Surface current distribution of the absorber design at (a) 380 THz, (b) 450 THz, (c) 525 THz and (d) 600 THz

3.4.2.2.3 Polarization and Incident Angle Analysis

In order to further analysis absorption behavior of proposed design regarding the radiation sources, numerical simulations under different incident angles for transverse electric (TE), transverse magnetic (TM) modes and for different polarization angles (TEM mode) are carried out. Absorption spectra for TE and TM modes with respect to frequency range of interest illustrated in Figure 3.22 and Figure 3.23.

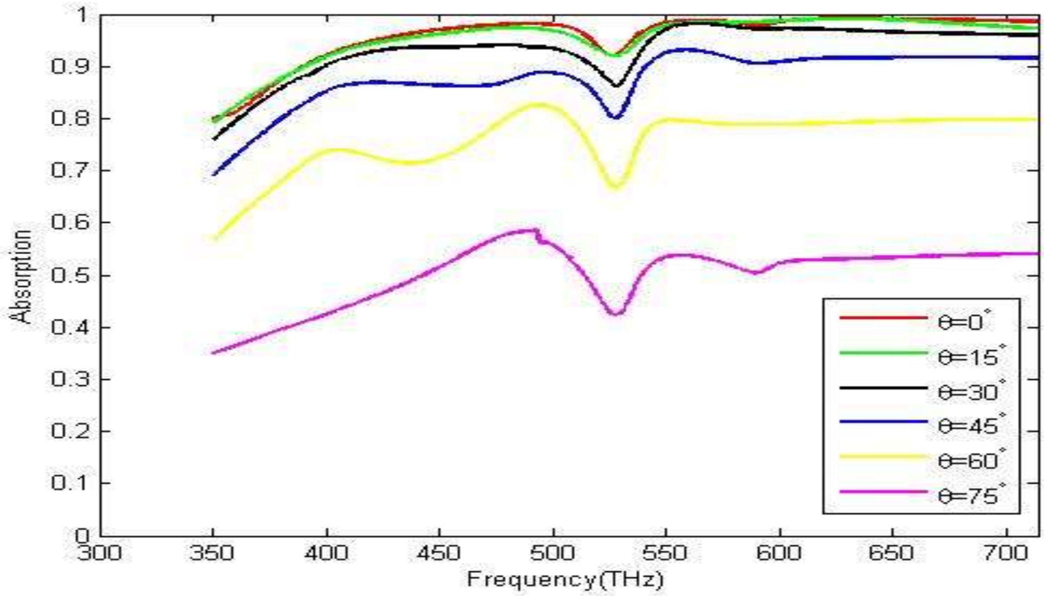

Figure 3.22 Simulated absorption spectra for different incident angles for TE mode.

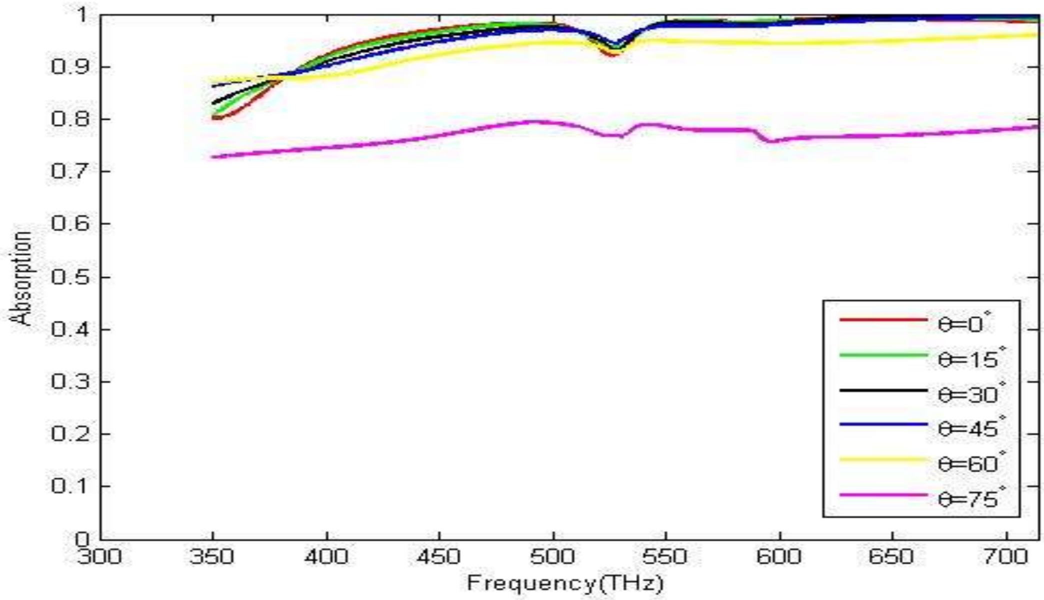

Figure 3.23 Simulated absorption spectra for different incident angles for TM mode.

From the results, it can be observed that the incident angles for TE mode highly sensitive than TM mode, especially for 60 degree and 75 degree whichs have minimum absorption rates. Incident wave which dependent of strength of magnetic field component has angle of incidence ‘‘θ ’’, which becomes smaller in case of θ increases. Thus, at larger incident angles such as 60 degree and 75 degree, the magnetic polaritons are not efficiently excited which increase reflection of incident waves and decrease amount of absorption by impedance mismatch. Absorption rate is achieved more than 90 % except for 60 degree and 75 degree.

Due to high symmetric characteristics of the design that we studied provides polarization independency under polarization angles (TEM mode) from 0 degree to 90 degree as shown in Figure 3.24. In this way, it can be expressed that proposed MXene based metamaterial absorber have ability to keep absorbance high without considering the polarization angles, so proposed design is a good candidate for solar cells.

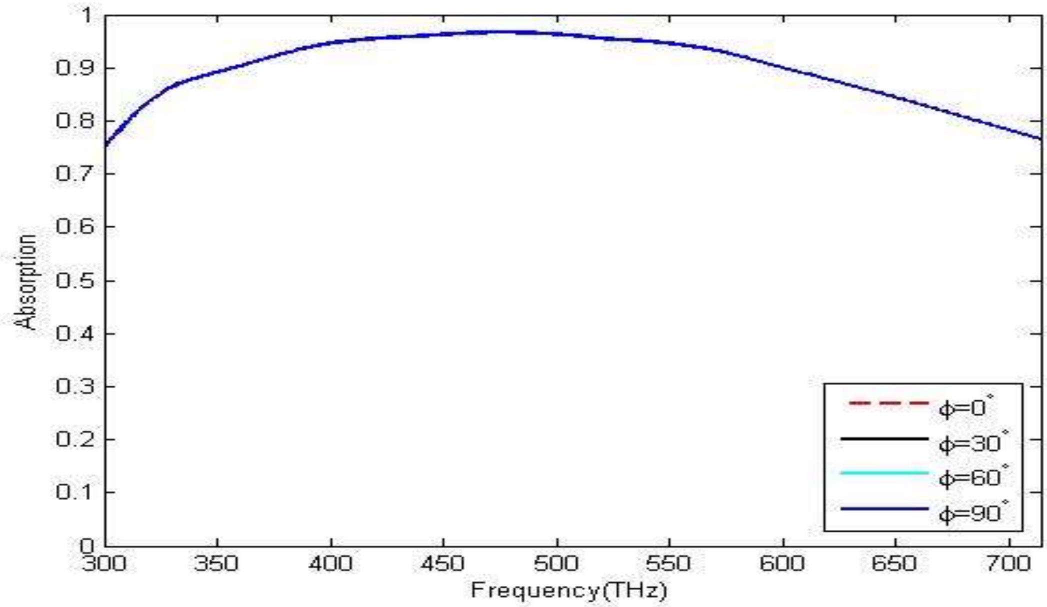

Figure 3.24 Simulated absorption spectra for different polarization angles at normal incidence for TEM mode.

CHAPTER 4

CONCLUSIONS AND FUTURE STUDIES

4.1 Conclusions

In this thesis, design and simulation of MXene based metamaterial has been investigated. Results of simulation analyzed for understand physics behind absorption. Geometric parameters study is done to show importance of geometric configuration of materials. Electric field, magnetic field and surface current distributions of proposed design are investigated at four different frequencies. Absorption behavior of proposed design regarding the radiation sources are studied. In addition numerical simulation under different angles for (TE) and (TM) modes are done. From the results of numerical simulation for different polarization angles (TEM) mode, we demonstrate that proposed design provide polarization angles independency and can be good candidate for solar cells. Now, we will mention summary of each chapters.

In the first chapter, types of energy source and consumption of this types of energy source by years are explained and analyzed. Also pointed to the increase the use of renewable energy sources over the years. Reasons of why solar cells have not yet reached a sufficient level of efficiency are explained. Some applications that using two dimensional material in the solar cell are specified.

Second chapter include description of solar cells and their details, types of solar cells and their efficiency. Also classification, types and applications of metamaterial are explained. Definition and types of two dimensional materials, information about MXene and photovoltaic applications of MXene are mentioned. Theoretical information about TE, TM, TEM mode and physics of absorption for solar cells are explained.

In the third chapter, visible light of electromagnetic spectrum is defined. Simulation software that we used during this study is introduced. Study that we used as a reference is analyzed with using computational and numerical simulation software. The proposed MXene based metamaterial absorber for solar cells is introduced with shape and geometrical dimensions. Material properties extraction of MXene film are specified. Design steps of proposed structure are explained with details.

In the last part of third chapter we reported the results of simulations which include absorption and reflection behavior of proposed design, absorption behavior of geometric parameters study, fields and surface current distributions of proposed design, absorption behavior of the design under different incident and polarization angles.

In order to design and investigate MXene based solar cell absorber, first we obtained real and imaginary parts of permittivity for MXene film. After that we added datas of permittivity versus frequency (terahertz) in material library of CST microwave studio. Due to the succesfull geometric configuration of structure, we reached maximum 96.8 % absorption at 450 THz.

The contribution of this study to the scientific literature is show that MXene can be used as a active material in solar cell absorber that reached 96.8 % absorption by means of CST microwave studio in the frequency range of 300 to 714 THz.

4.2 Future Studies

In the introduction parts of this thesis, we mentioned about usage of solar energy in the world that increased by the years. The ratio of increases is not so fast because of efficiency of solar cells is not in the sufficient level. From this point of view, we designed and simulated a MXene based absorber to absorb electromagnetic waves that solar cells need to increase efficiency of solar cells. In this way, further studies in future can be analyze the efficiency of the solar cells by integrating the MXene based absorber into the solar cells. This point of view can open a way to fabricate high efficiency solar cells which can increase the use of renewable energy.

REFERENCES

[1] Read, S., Lindhult, E., & Mashayekhi, A. (2016). The Inefficiencies of Energy Efficiency: Reviewing the Strategic Role of Energy Efficiency and its Effectiveness in Alleviating Climate Change. *Journal of Settlements and Spatial Planning*, 2016(Spec. Iss. **5**), 77-87.

[2] Simon, A. L. (2013). Energy Resources. Elsevier.

]3] Ritchie, H., Roser, M. (2018). Energy production & changing energy sources. OurWorldInData. *org*.

[4] Belmili, H., Haddadi, M., Bacha, S., Almi, M. F., Bendib, B. (2014). Sizing stand-alone photovoltaic-wind hybrid system: Techno-economic analysis and optimization. *Renewable and Sustainable Energy Reviews*, **30**, 821-832.

[5] Chou, P. H., & Kim, S. (2010, April). Techniques for maximizing efficiency of solar energy harvesting systems. In *Proceedings of the 5th Conference on Mobile Computing and Ubiquitous Networking, Seattle, WA, USA* (Vol. 2628, p. 139145).

[6] Sahin, G. (2016). Effect of wavelength on the electrical parameters of a vertical parallel junction silicon solar cell illuminated by its rear side in frequency domain. *Results in physics*, **6**, 107-111.

[7] Geng, D., Yang, H. Y. (2018). Recent advances in growth of novel 2D materials: beyond graphene and transition metal dichalcogenides. *Advanced Materials*, **30(45)**, 1800865.

[8] Rufangura, P., Sabah, C. (2017). Graphene-based wideband metamaterial absorber for solar cells application. *Journal of Nanophotonics*, **11(3)**, 036008.

[9] Obaidullah, M., Esat, V., Sabah, C. (2017). Thin film (6, 5) semiconducting single-walled carbon nanotube metamaterial absorber for photovoltaic applications. *Optical Engineering*, **56(12)**, 127101.

[10] Choi, W., Choudhary, N., Han, G. H., Park, J., Akinwande, D., Lee, Y. H. (2017). Recent development of two-dimensional transition metal dichalcogenides and their applications. *Materials Today*, **20(3)**, 116-130.

[11] Guo, Z., Gao, L., Xu, Z., Teo, S., Zhang, C., Kamata, Y., Ma, T. (2018). High Electrical Conductivity 2D MXene Serves as Additive of Perovskite for Efficient Solar Cells. *Small*, **14(47)**, 1802738.

[12] Dall'Agnese, C., Dall'Agnese, Y., Anasori, B., Sugimoto, W., Mori, S. (2018). Oxidized Ti 3 C 2 MXene nanosheets for dye-sensitized solar cells. *New Journal of Chemistry*, ***42*****(20)**, 16446-16450.

[13] Mulla, B., Sabah, C. (2016). Multiband metamaterial absorber design based on plasmonic resonances for solar energy harvesting. *Plasmonics*, **11(5)**, 1313-1321.

[14] Voss, B., Knobloch, T., Goetzberger, A. (1998). Crystalline silicon solar cells.

[15] Rajput, S. K. Fundamentals, Economic and Energy Analysis.

[16] Würfel, P., Würfel, U. (2016). *Physics of solar cells: from basic principles to advanced concepts.* John Wiley & Sons.

[17] Zhang, X., Lau, S. K., Lau, S. S. Y., Zhao, Y. (2018). Photovoltaic integrated shading devices (PVSDs): A review. *Solar Energy*, **170**, 947-968.

[18] Abass, A. (2014*). Light absorption enhancement and electronic properties of thin-film solar cells* (Doctoral dissertation, Ghent University).

[19] Green MA, Hishikawa Y, Dunlop ED, et al. Solar cell efficiency tables (Version 53). *Prog Photovolt Res Appl.* 2019;**27:3**–12.

[20] Berney Needleman, D. (2014). *Optical design guidelines for spectral splitting photovoltaic systems: A sensitivity analysis approach* (Doctoral dissertation, Massachusetts Institute of Technology).

[21] Kasap, S., Capper, P. (Eds.). (2017). *Springer handbook of electronic and photonic materials*. Springer.

[22] Singh, G., Marwaha, A. (2015). A review of metamaterials and its applications.

[23] Cheng, D. K. (1989). *Field and wave electromagnetics*. Pearson Education India.

[24] Balanis, C. A. (1999). *Advanced engineering electromagnetics*. John Wiley & Sons.

[25] Lehner, G. (2010). *Electromagnetic field theory for engineers and physicists*. Springer Science & Business Media.

[26] Liu, Y., Chen, Y., Li, J., Hung, T. C., Li, J. (2012). Study of energy absorption on solar cell using metamaterials. *Solar energy*, **86(5)**, 1586-1599.

[27] Ouyang, M., Huang, J. L., Cheung, C. L.,Lieber, C. M. (2001). Atomically resolved single-walled carbon nanotube intramolecular junctions. *Science*, **291(5501)**,97-100.

[28] Eatemadi, A., Daraee, H., Karimkhanloo, H., Kouhi, M., Zarghami, N., Akbarzadeh, A., Joo, S. W. (2014). Carbon nanotubes: properties, synthesis, purification, and medical applications. *Nanoscale research letters*, **9(1)**, 393.

[29] Grobert, N. (2007). Carbon nanotubes–becoming clean. *Materials today*, **10(1-2)**, 28-35.

[30] Ganesh, E. N. (2013). Single walled and multi walled carbon nanotube structure, synthesis and applications. *International Journal of Innovative Technology and Exploring Engineering*, ***2*(4)**, 311-320.

[31] Berger, M. (2009). *Nano-society: pushing the boundaries of technology* (Vol. 8). Royal Society of Chemistry.

[32] Kumar, S., Schwingenschlögl, U. (2016). Thermoelectric performance of functionalized Sc 2 C MXenes. *Physical Review B*, **94(3)**, 035405.

[33] Fu, Y. D., Wang, B., Teng, Y., Zhu, X. S., Feng, X. X., Yan, M. F., Sun, W. (2017). The role of group III, IV elements in Nb 4 AC 3 MAX phases (A= Al, Si, Ga, Ge) and the unusual anisotropic behavior of the electronic and optical properties. *Physical Chemistry Chemical Physics*, **19(23)**, 15471-15483.

[34] Chaudhari, N. K., Jin, H., Kim, B., San Baek, D., Joo, S. H., Lee, K. (2017). MXene: an emerging two-dimensional material for future energy conversion and storage applications. *Journal of Materials Chemistry* A, **5(47)**, 24564-24579.

[35] Yu, Y. X. (2016). Prediction of mobility, enhanced storage capacity, and volume change during sodiation on interlayer-expanded functionalized Ti3C2 MXene anode materials for sodium-ion batteries. *The Journal of Physical Chemistry C*, **120(10)**, 5288-5296.

[36] Ma, S., Yuan, D., Jiao, Z., Wang, T., Dai, X. (2017). Monolayer Sc2CO2: a promising candidate as a SO2 gas sensor or capturer. *The Journal of Physical Chemistry C*, **121(43)**, 24077-24084.

[37] Yadav, A., Dashora, A., Patel, N., Miotello, A., Press, M., Kothari, D. C. (2016). Study of 2D MXene Cr2C material for hydrogen storage using density functional theory. *Applied Surface Science*, **389**, 88-95.

[38] Kang, Z., Ma, Y., Tan, X., Zhu, M., Zheng, Z., Liu, N., Gao, Y. (2017). MXene–Silicon Van Der Waals Heterostructures for High-Speed Self-Driven Photodetectors. *Advanced Electronic Materials*, ***3*(9)**, 1700165.

[39] Chaudhuri, K., Alhabeb, M., Wang, Z., Shalaev, V. M., Gogotsi, Y., Boltasseva, A. (2018). Highly broadband absorber using plasmonic titanium carbide (MXene). *ACS Photonics*, ***5*(3)**, 1115-1122.

[40] Yang, L., Dall'Agnese, Y., Hantanasirisakul, K., Shuck, C. E., Maleski, K., Alhabeb, M., Shen, L. (2019). SnO 2–Ti 3 C 2 MXene electron transport layers for perovskite solar cells. *Journal of Materials Chemistry A*, ***7*(10)**, 5635-5642.

[41] Avouris, P. (2010). Graphene: electronic and photonic properties and devices. *Nano letters*, **10(11)**, 4285-4294.

[42] Xia, F., Wang, H., Xiao, D., Dubey, M., Ramasubramaniam, A. (2014). Two-dimensional material nanophotonics. *Nature Photonics*, ***8*(12)**, 899.

[43] Pant, A., Mutlu, Z., Wickramaratne, D., Cai, H., Lake, R. K., Ozkan, C., Tongay, S. (2016). Fundamentals of lateral and vertical heterojunctions of atomically thin materials. *Nanoscale*, ***8*****(7)**, 3870-3887.

[44] Mak, K. F., Ju, L., Wang, F., Heinz, T. F. (2012). Optical spectroscopy of graphene: From the far infrared to the ultraviolet. *Solid State Communications*, **152(15)**, 1341-1349.

[45] Sharma, S., Jain, K. K., Sharma, A. (2015). Solar cells: in research and applications-a review. *Materials Sciences and Applications*, **6(12)**, 1145.

[46] Saga, T. (2010). Advances in crystalline silicon solar cell technology for industrial mass production. *npg asia materials*, ***2*****(3)**, 96.

[47] Işık, F. (2008). *Elektromanyetik Darbelerden Korunma* (Doctoral dissertation, Fen Bilimleri Enstitüsü).

[48] Wang, L. (2010). Investigation of carbon nanotube properties and applications at microwave and THz frequencies.

[49] Chaudhuri, K., Alhabeb, M., Wang, Z., Shalaev, V. M., Gogotsi, Y., Boltasseva, A. (2018). Highly broadband absorber using plasmonic titanium carbide (MXene). *ACS Photonics*, **5(3)**, 1115-1122.

[50] Mulla, B., Sabah, C. (2015). Perfect metamaterial absorber design for solar cell applications. *Waves in Random and Complex Media*, **25(3)**, 382-392.

[51] Ustunsoy, M. P., Sabah, C. (2016). Dual-band high-frequency metamaterial absorber based on patch resonator for solar cell applications and its enhancement with graphene layers. *Journal of Alloys and Compounds*, **687**, 514-520.

[52] Zouaghi, W., Voß, D., Gorath, M., Nicoloso, N., & Roskos, H. G. (2015). How good would the conductivity of graphene have to be to make single-layer-graphene metamaterials for terahertz frequencies feasible?. *Carbon*, **94**, 301-308.

[53] Rufangura, P., Sabah, C. (2016). Design and characterization of a dual-band perfect metamaterial absorber for solar cell applications. *Journal of Alloys and Compounds*, **671**, 43-50.

[54] EMEKLI, N. Y., CAGLAYAN, N., OZMERZI, A., CANAKCI, M. (2012). Structural characteristics and heat requirements of modern greenhouses in southern of Turkey. *Journal of the Faculty of Agriculture of Akdeniz University* (Turkey).

[55] Perron, B., Stearns, A. (2010). A review of a presentation technology: Prezi.